AGU PUBLICATIONS

JGR

Journal of Geophysical Research: Oceans

RESEARCH ARTICLE

10.1002/2017JC012691

This article is a companion to *Li et al.* [2017], doi:10.1002/2017JC012692.

Key Points:
- Intraseasonal variability of the mixed-layer depth (MLD) and barrier layer thickness (BLT) during MISO events is investigated
- MISOs induce in-phase variations in MLD and isothermal layer depth, and variation of BLT is relatively small
- MLD deepening is caused by wind stress through turbulent mixing and surface salinity change while the ILD deepening is driven by heat flux

Supporting Information:
- Supporting Information S1

Correspondence to:
Y. Li,
yuanlong.li@colorado.edu

Citation:
Li, Y., W. Han, M. Ravichandran, W. Wang, T. Shinoda, and T. Lee (2017), Bay of Bengal salinity stratification and Indian summer monsoon intraseasonal oscillation: 1. Intraseasonal variability and causes, *J. Geophys. Res. Oceans*, *122*, 4291–4311, doi:10.1002/2017JC012691.

Received 9 JAN 2017
Accepted 30 APR 2017
Accepted article online 4 MAY 2017
Published online 23 MAY 2017

Bay of Bengal salinity stratification and Indian summer monsoon intraseasonal oscillation: 1. Intraseasonal variability and causes

Yuanlong Li[1], Weiqing Han[1], M. Ravichandran[2], Wanqiu Wang[3], Toshiaki Shinoda[4], and Tong Lee[5]

[1]Department of Atmospheric and Oceanic Sciences, University of Colorado, Boulder, Colorado, USA, [2]National Centre for Antarctic and Ocean Research, Vasco da Gama, India, [3]Climate Prediction Center, NOAA/NWS/NCEP, College Park, Maryland, USA, [4]Department of Physical and Environmental Sciences, Texas A&M University, Corpus Christi, Texas, USA, [5]Jet Propulsion Laboratory, California Institute of Technology, Pasadena, California, USA

Abstract The huge freshwater flux of the Indian summer monsoon (ISM; May–October) gives rise to strong salinity stratification in the Bay of Bengal (BoB), causing a shallow mixed layer and a thick barrier layer, which potentially affects intraseasonal oscillations of the monsoon (MISOs). In this study, intraseasonal variability of the mixed-layer depth (MLD) and barrier layer thickness (BLT) is investigated using in situ observations from Argo floats and moored buoys and an ocean general circulation model (OGCM). The average MLD in the BoB is typically 20–30 m during the ISM, while the BLT increases from ~10 m in May–June to 20–40 m in September–October. MISOs induce in-phase variations in MLD and isothermal layer depth (ILD), both of which are deepened by 8–15 m during MISO active phase, while the change of BLT is small and within the error range of Argo data sampling. In the northern (southern) bay, BLT increases by ~5 m (2 m) during MISOs owing to a larger deepening of ILD than MLD. OGCM experiments are performed to understand the underlying mechanism. In the BoB intraseasonal variations of MLD, ILD and BLT arise largely from ocean internal instability, whereas those induced by MISOs are weaker. The in-phase variations of MLD and ILD during MISOs are induced by different processes. The MLD deepening is primarily caused by wind stress forcing, while the ILD deepening is driven by surface heat fluxes via surface cooling. The limited variability of BLT is due to the offsetting of different forcing processes.

1. Introduction

In boreal summer, the northward propagating monsoon intraseasonal oscillation (MISO) [*Yasunari*, 1980; *Krishnamurti and Subrahmanyam*, 1982] is the major mode of intraseasonal variability in the tropical troposphere over the Asian monsoon region. In the Indian Ocean basin, it is characterized by 30–60 day fluctuations of convection and low-level winds, propagating from the equator to South Asian and Southeast Asian region. The MISO induces prominent intraseasonal variability in the Indian summer monsoon (ISM) rainfall, manifesting as the fluctuations between active spells with good rainfall and break spells with little rainfall [*Goswami and Ajaya Mohan*, 2001; *Webster et al.*, 2002]. The complex variability at intraseasonal timescale brings difficulties for an accurate prediction of the ISM rainfall [e.g., *Webster et al.*, 1998; *Wang et al.*, 2005] that is of supreme importance for the agricultural planning and socioeconomic activities of the large populations living in this region [e.g., *Parthasarathy et al.*, 1994; *Gadgil and Rupa Kumar*, 2006; *Turner and Annamalai*, 2012]. Strong MISO events also play a major role in triggering the monsoon onset, producing the extreme flood/drought events, and modulating the intensity and duration of the monsoon [e.g., *Lau and Yang*, 1996; *Annamalai and Slingo*, 2001; *Hoyos and Webster*, 2007]. In this regard, understanding the physical processes associated with the MISO is critical for improving model simulation and prediction of the ISM rainfall.

The importance of air-sea interaction in the MISO dynamics has been increasingly recognized in recent researches. Covariance between sea surface temperature (SST) and atmospheric convection during MISO events was reported by many observational studies and believed to be important for MISO evolution [e.g., *Sengupta and Ravichandran*, 2001; *Sengupta et al.*, 2001; *Vecchi and Harrison*, 2002; *Duvel and Vialard*, 2007].

Significant influence of SST on MISO convection was confirmed by modeling studies [*Fu et al*., 2002, 2003; *Rajendran and Kitoh*, 2006; *Seo et al*., 2007; *Achuthavarier and Krishnamurthy*, 2011]. Taking into account intraseasonal air-sea interaction, coupled general circulation models (GCMs) produce more realistic MISOs in amplitude, frequency, structure, and propagation behaviors than atmosphere-only GCMs and achieve a higher prediction skill for the ISM rainfall [e.g., *Waliser et al*., 2001; *Fu et al*., 2003, 2008; *Fu and Wang*, 2004; *Seo et al*., 2007; *Wang et al*., 2009]. On its pathway from the equator to South Asia, the MISO is affected by the underlying SST variability in the Bay of Bengal (BoB). Large-scale warm SST anomalies are usually observed prior to the active phase of MISO, which contributes to organization of the convection system and facilitates its northward movement [*Sengupta et al*., 2001; *Kemball-Cook and Wang*, 2001; *Joseph and Sabin*, 2008]. Cool SST anomalies, on the other hand, can lead to abrupt monsoon breaks [*Vecchi and Harrison*, 2002]. These SST anomalies are however generated by complex mechanisms, involving mixed effects of surface atmospheric forcing and ocean internal instabilities [e.g., *Jochum and Murtugudde*, 2005; *Duncan and Han*, 2009; *Vialard et al*., 2012]. More effort is required to explore the upper-ocean processes controlling intraseasonal SST variability.

With the development of the ISM, heavy rainfall and enhanced discharge of major rivers such as the Ganges-Brahmaputra and the Irrawaddy lead to dramatic surface freshening within the BoB, from $>$32.0 to $<$30.0 psu in sea surface salinity (SSS) [*Han and McCreary*, 2002; *Shenoi et al*., 2002; *Vinayachandran et al*., 2013], resulting in sharp salinity stratification near the sea surface [e.g., *Rao and Sivakumar*, 2003; *Sengupta et al*., 2016]. Near-surface density stratification is therefore mainly controlled by salinity, giving rise to a shallow surface mixed-layer depth (MLD) and a thick barrier layer [*Vinayachandran et al*., 2002; *Thadathil et al*., 2007; *Felton et al*., 2014]. The salinity stratification can therefore have a twofold impact on SST. While the shallow MLD traps the atmospheric fluxes and leads to enhanced SST variability, the barrier layer suppresses the heat exchange between the warm mixed layer and the cold thermocline, which is essential for maintaining the high SST and convective activity during the ISM [e.g., *Sprintall and Tomczak*, 1992; *Shenoi et al*., 2002; *Neetu et al*., 2012; *Thadathil et al*., 2016].

Both MLD and barrier layer thickness (BLT) are important factors in determining the amplitude of intraseasonal SST variability [e.g., *Sengupta and Ravichandran*, 2001; *Schiller and Godfrey*, 2003; *Drushka et al*., 2014; *Li et al*., 2014, 2016]. *Waliser et al*. [2004] and *Duvel and Vialard* [2007] showed that strong intraseasonal SST anomalies tend to occur in regions with a shallow MLD. *Roxy et al*. [2013] suggested that the MLD over the tropical Indian Ocean modulates not only intraseasonal SST but also air-sea interaction of MISOs. *Li et al*. [2016] showed that the shallow MLD in the Arabian Sea in May–July significantly enhances the intraseasonal SST variability and thereby contributes to the strong MISO events during the ISM onset. The barrier layer affects intraseasonal SST primarily through vertical entrainment [*Schiller and Godfrey*, 2003; *Drushka et al*., 2014]. *Duncan and Han* [2009] speculated that the thick barrier layer in the BoB can reduce entrainment cooling magnitude and thus influence SST anomalies. Despite these findings, our knowledge of the role played by the BoB salinity stratification in MISO development remains limited and fragmental. This is to a large extent due to the lack of observations and difficulties in model simulation. Subsurface ocean observations are rather sparse. Although pronounced intraseasonal variations in MLD and BLT are recorded by several buoys and floats [*Parampil et al*., 2010; *Girishkumar et al*., 2011, 2013], these observations are contaminated by strong signals of eddies and internal waves. Meanwhile, model simulation of MLD and BLT in rainfall-rich regions is still a challenging task for the present generation of ocean GCMs (OGCMs) [e.g., *Duncan and Han*, 2009; *Li et al*., 2013, 2015; *Felton et al*., 2014; *Keerthi et al*., 2016]. The ability to simulate sharp near-surface salinity stratification is dependent upon the accuracy of surface freshwater flux, vertical resolution, parameterization schemes for turbulent mixing and double diffusion, as well as many other aspects of the model. Large biases in tropical MLD and BLT are quite common among the "state-of-the-art" climate models [e.g., *Turner et al*., 2012; *Roxy et al*., 2013; *Huang et al*., 2014], which may cause large errors in the simulated SST and air-sea fluxes. From this point of view, a reliable evaluation of the salinity stratification effect on important climate modes, such as the MISO, is of interest for both the ocean and climate research communities.

In this study we make the first attempt to provide a comprehensive investigation for the role of the BoB salinity stratification, which is represented by the MLD and BLT, in the MISO variability, taking advantage of the recently amassed in situ observations from the global Argo float array [*Roemmich et al*., 2009] and eddy-permitting OGCM simulations forced with high-quality satellite-derived atmospheric data sets. The results

are presented in two parts. As Part 1, this paper focuses on the MLD and BLT variations during MISO events to reveal their spatial-temporal features and causes. Impacts of MLD and BLT on SST and convection variabilities of the MISO are assessed in Part 2 [*Li et al*., 2017]. The rest of Part 1 is organized as follows. In section 2, we introduce the observational data sets and the OGCM utilized in this study. In section 3, we describe the observed and OGCM-simulated variations of MLD and BLT during the ISM, including both seasonal evolution and intraseasonal variability, and validation of the OGCM performance. In section 4, the OGCM experiments isolating different processes are analyzed to explore the causes of MLD and BLT variability. Section 5 provides a summary and discussion for the primary findings of the paper.

2. Data and Model

2.1. Data and Methods

The primary data used for estimating the MLD and BLT are the Argo data profiles from January 2005 through December 2015 (before 2005 there were fewer Argo profiles), obtained from the Coriolis Global Data Acquisition Center of France. These data have undergone automatic preprocessing and sophisticated quality control procedures by the Argo science team [*Owens and Wong*, 2009]. The Argo floats measure temperature and salinity typically from ~5 to ~2000 dbar every 10 days with a vertical interval of ~5 dbar near the sea surface. Obvious bad records, such as temperature falling outside the 0–35°C temperature range or 28.0–38.0 psu salinity range, were removed. Additionally, profiles meeting the criteria of (1) no valid data in the upper 8 dbar or (2) data gaps exceeding 25 dbar in the upper 150 dbar were excluded, which account for 4.4% of the total profile number. After the above processing, there were 32,427 usable profiles during boreal summer (May–October) in the study region of 50°E–105°E, 10°S–26°N (Figure 1a). The profiles in the Arabian Sea, BoB, and eastern equatorial Indian basin are more abundant comparing to other areas of the Indian Ocean. In the BoB interior, more than 40 profiles are available for a 1° × 1° grid box. In the BoB box, defined over 85°E–95°E, 7°N–21°N, which is important for our investigation, there are 5147 profiles during May–October. At some grids, profile number can exceed 70, 80, or even 90. In each summer of 2005–2015, we can find at least 2400 profiles (Figure 1b). The period of 2010–2013 witnessed an evident increase in profile number, thanks to the increased float deployments. Regarding the seasonality, the profiles are approximately evenly distributed among the 6 months of May–October (Figure 1c). Over tropics there is large day-to-night variation in near-surface stratification. Figure 1d shows the profile distribution over the 24 h of the day, suggesting no significant bias in daytime or nighttime sampling.

For each selected profile, temperature and salinity data were linearly interpolated into 1 m vertical intervals between 5 and 200 m. In this study, the MLD is defined as the depth at which the potential density increase

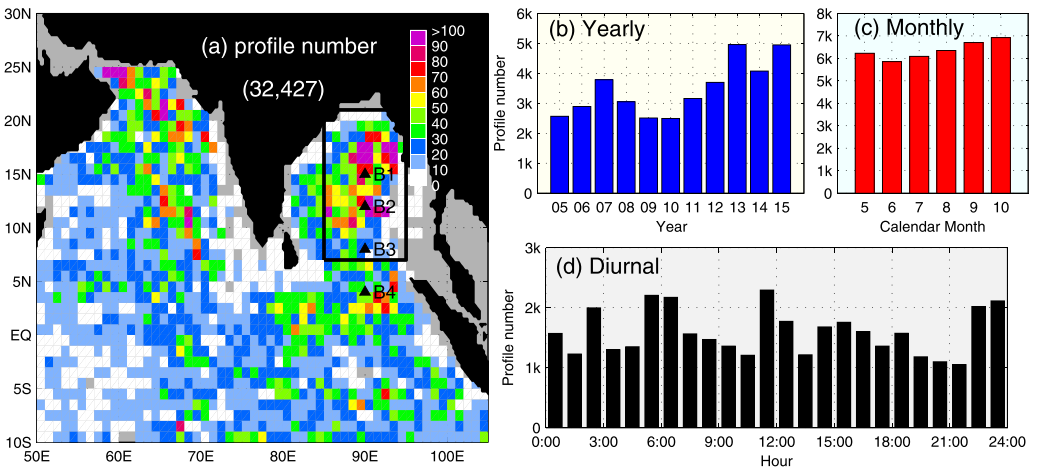

Figure 1. Distribution of Argo profiles during May–October of 2005–2015. There are in all 32,427 valid profiles in the region of 50°E–105°E, 10°S–26°N. Figure 1a shows the Argo profile number in 1° × 1° box, Figures 1b–1d show the yearly (interannual), monthly (seasonal), and hourly (diurnal) distributions, respectively. The black rectangle defines the BoB box (85°E–95°E, 7°S–21°N). Black triangles denote the locations of the four RAMA buoys, B1 (90°E, 15°N), B2 (90°E, 12°N), B3 (90°E, 8°N), and B4 (90°E, 4°N).

$\Delta\sigma$ from the surface value is equivalent to a temperature decrease by $\Delta T = 0.5$°C [*de Boyer Montégut et al*., 2004],

$$\Delta\sigma = \sigma(T_S - \Delta T, S_S, P_S) - \sigma(T_S, S_S, P_S), \quad (1)$$

where T_S, S_S, and P_S are the surface values of temperature, salinity, and pressure, respectively. For profiles with (without) the 5 m data, the 5 m (shallowest) σ is taken as the surface value. The isothermal layer depth (ILD) is defined as the depth with a temperature decrease of $\Delta T = 0.5$°C from T_S. The BLT is calculated as the difference between ILD and MLD, i.e., BLT = ILD – MLD. For cases of ILD < MLD, BLT is set to be zero.

Besides Argo data, we also utilize the in situ measurements during 2008–2015 by four moored buoys from the Research Moored Array for African-Asian-Australian Monsoon Analysis and Prediction (RAMA) array [*McPhaden et al*., 2009] along 90°E at 15°N (B1), 12°N (B2), 8°N (B3), and 4°N (B4) (black triangles in Figure 1a). In the upper 100 m, salinity was measured at 1, 10, 20, 40, 60, and 100 m, while temperature was measured at 1, 10, 13, 20, 40, 60, 80, and 100 m depths. These data were also vertically interpolated into 1 m intervals, and then MLD, ILD, and BLT were computed in the same manner as for Argo data. Other ocean and atmosphere data sets analyzed in the study include the objectively analyzed 1°-grid monthly temperature and salinity climatology of World Ocean Atlas 2013 (WOA13) version 2 [*Locarnini et al*., 2013; *Zweng et al*., 2013] for 1955–2012, the 1° × 1° daily 7 day moving-average SSS data of the Aquarius/SAC-D Combined Active-Passive retrieval (CAP) version 4.0 product [*Lagerloef et al*., 2008; *Yueh et al*., 2014] for the period of August 2011 to May 2015, the 0.25° × 0.25° daily precipitation of the Tropical Rainfall Measuring Mission (TRMM) Multi-Satellite Precipitation Analysis (TMPA) level 3B42 V7 product [*Huffman et al*., 2007], the 0.25° × 0.25° daily 10 m winds from the Cross-Calibrated Multiplatform (CCMP) ocean 10 m wind vectors v1.1 [*Atlas et al*., 2010] for 2002–2011, the 0.25° × 0.25° gridded daily surface wind fields of the Advanced Scatterometer (ASCAT) satellite measurements [*Bentamy and Croize-Fillon*, 2012] for 2012–2014, and the geostationary enhanced 1° × 1° daily shortwave and longwave radiations (SWR and LWR) products of Clouds and the Earth's Radiant Energy System (CERES) [*Wielicki et al*., 1996; *Loeb et al*., 2001].

2.2. HYCOM

The OGCM used in this study is the Hybrid Coordinate Ocean Model (HYCOM) version 2.2.18 [*Halliwell*, 2004]. HYCOM is configured to the Indian Ocean basin between 30°E and 122.5°E, 50°S and 30°N with a horizontal resolution of 0.25° × 0.25° and 26 hybrid vertical layers [*Li et al*., 2014, 2015]. The layer thickness is ~2.9 m near the sea surface. Five degree sponge layers are applied at the western, eastern, and southern open-ocean boundaries, where the model temperature and salinity are relaxed to the WOA climatology. The diffusion/mixing parameters are identical to those used in *Li et al*. [2013]. The surface forcing fields of HYCOM include 0.75° × 0.75° 2 m air temperature and humidity from the European Centre for Medium-Range Weather Forecasts (ECMWF) Re-analysis Interim (ERA-Interim) products [*Dee et al*., 2011], 1° × 1° surface net SWR and LWR from CERES product, precipitation of TRMM TMPA level 3B42 V7 product, and surface wind speed and wind stress computed with CCMP v1.1 10 m winds. In our model configuration, wind speed and wind stress are fed separately to the model. Wind stress affects the model ocean through driving advection, upwelling, and turbulent mixing, while wind speed affects the ocean mainly through evaporation and turbulent heat flux (latent heat flux plus sensible heat flux). Instead of prescribing, the HYCOM computes evaporation and turbulent heat fluxes with wind speed, air temperature, specific humidity, and model SST at each time step using the Coupled Ocean-Atmosphere Response Experiment (COARE 3.0) algorithm [*Kara et al*., 2005]. In addition, for river discharges, we use the satellite-based monthly discharge records of the Ganga-Brahmaputra [*Papa et al*., 2010] and monthly discharge data of *Dai et al*. [2009] for other BoB rivers as the lateral freshwater flux.

The HYCOM was spun up from a state of rest for 30 years, forced with monthly climatology of the aforementioned fields. After the spin-up, the model is integrated forward from March 2000 to December 2011 with daily atmospheric forcing, and the wind forcing is from CCMP v1.1 data. The CCMP v1.1 wind data after December 2011 was not available when the model experiments were conducted. We therefore used ASCAT surface winds to extend the model experiment to December 2014. We conducted a comprehensive comparison between the CCMP and ASCAT winds for their overlapping period (2008–2011) and found a good consistency in variability at various timescales over the tropical Indian Ocean (figures not shown). The 2000–2014 simulation described above is named as the main run (MR), and its outputs are stored in both daily mean and 3 day mean versions. To exclude the transient effect from the spin-up run, we discard the

output of 2000 and 2001, and the 13 year data of 2002–2014 are used for our analysis. As shown in our previous studies [*Li et al.*, 2014, 2015, 2016], HYCOM MR can realistically represent the upper-layer mean state and intraseasonal variability in the tropical Indian Ocean, including SST, SSS, and ocean circulation. Therefore in this paper additional validation is carried out only for ocean stratification (MLD, BLT, ILD, and thermocline depth) over the BoB (section 3). To understand the physical processes affecting ocean salinity stratification, we performed another five parallel experiments for 2000–2014, which are described in section 4.1.

3. Variations of MLD and BLT

Measurements by RAMA buoys at B1, B3, and B4 reveal pronounced variations of stratification in the BoB, showing large-amplitude variability in MLD and ILD at both seasonal and intraseasonal timescales (Figure 2). At B1 in the northern BoB (15°N), the seasonal difference reaches 40 m in MLD and 80 m in ILD (Figure 2a). In boreal summer, intraseasonal fluctuations of MLD and ILD, such as those seen in May–September 2013, can also exceed 20 m. At B3 and B4 (8°N and 4°N), intraseasonal fluctuations larger than 20 m are also found (Figures 2b and 2c). These MLD and ILD changes lead to variations of BLT, with intraseasonal spikes of 10–30 m at all the three buoys superimposed on the strong seasonal cycle (Figure 2d). The mean state and seasonal variation are the background over which intraseasonal variability develops, and they can affect intraseasonal variability due to nonlinear nature of the ocean stratification. Before investigating intraseasonal variability, we first briefly examine the mean state and seasonal variation of the BoB from Argo observation and HYCOM simulation.

3.1. Mean State and Seasonal Variations

Climatological MLD, ILD, and BLT fields for the ISM season (May–October) are obtained by mapping the Argo data samples of 2005–2015 onto 1° × 1° grids and compared with WOA13 climatology and HYCOM MR simulation in Figure 3. The BoB is characterized by a shallow MLD (20–40 m) and a large BLT (10–30 m), in comparison with other regions of the Indian Ocean. The three data sets are overall consistent in large-scale structures. There are however some apparent quantitative regional differences. For MLD and ILD, the Argo-based maps share more common features with HYCOM than with WOA13. Over most part of the tropical Indian Ocean the WOA13 has shallower MLD and ILD than the other two. This could be partially due to

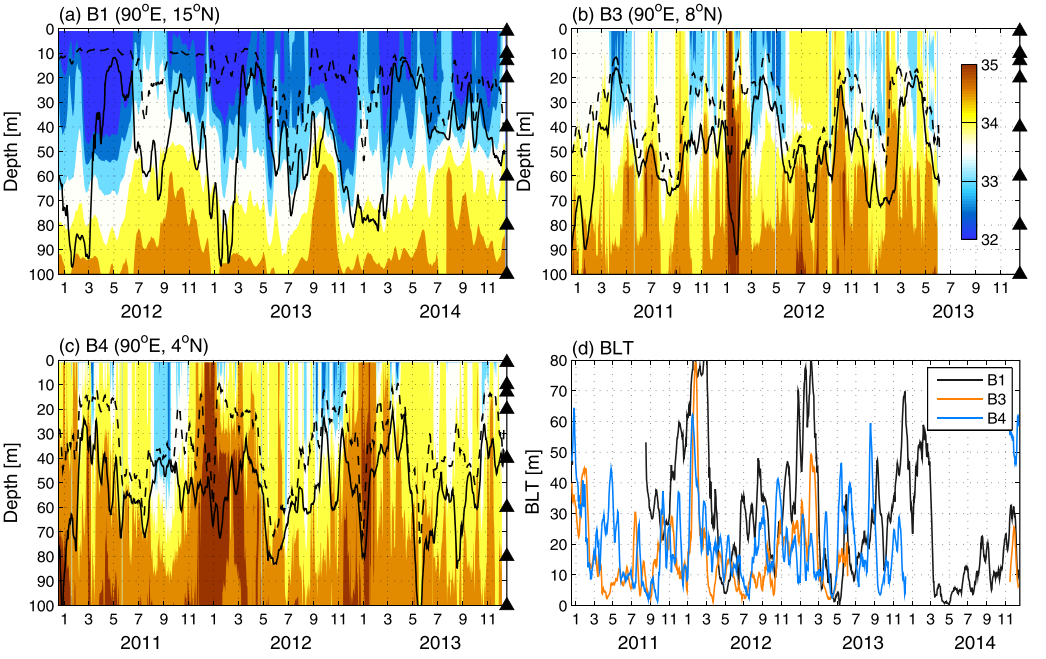

Figure 2. Daily salinity (color shading; in psu), MLD (dashed curve), and ILD (solid curve) measured by RAMA buoys (a) B1, (b) B3, and (c) B4. Black triangles mark the depths of measurement sensors. (d) BLT time series (m) from B1, B3, and B4. Here MLD, ILD, and BLT were smoothed with a 10 day running mean before plotting.

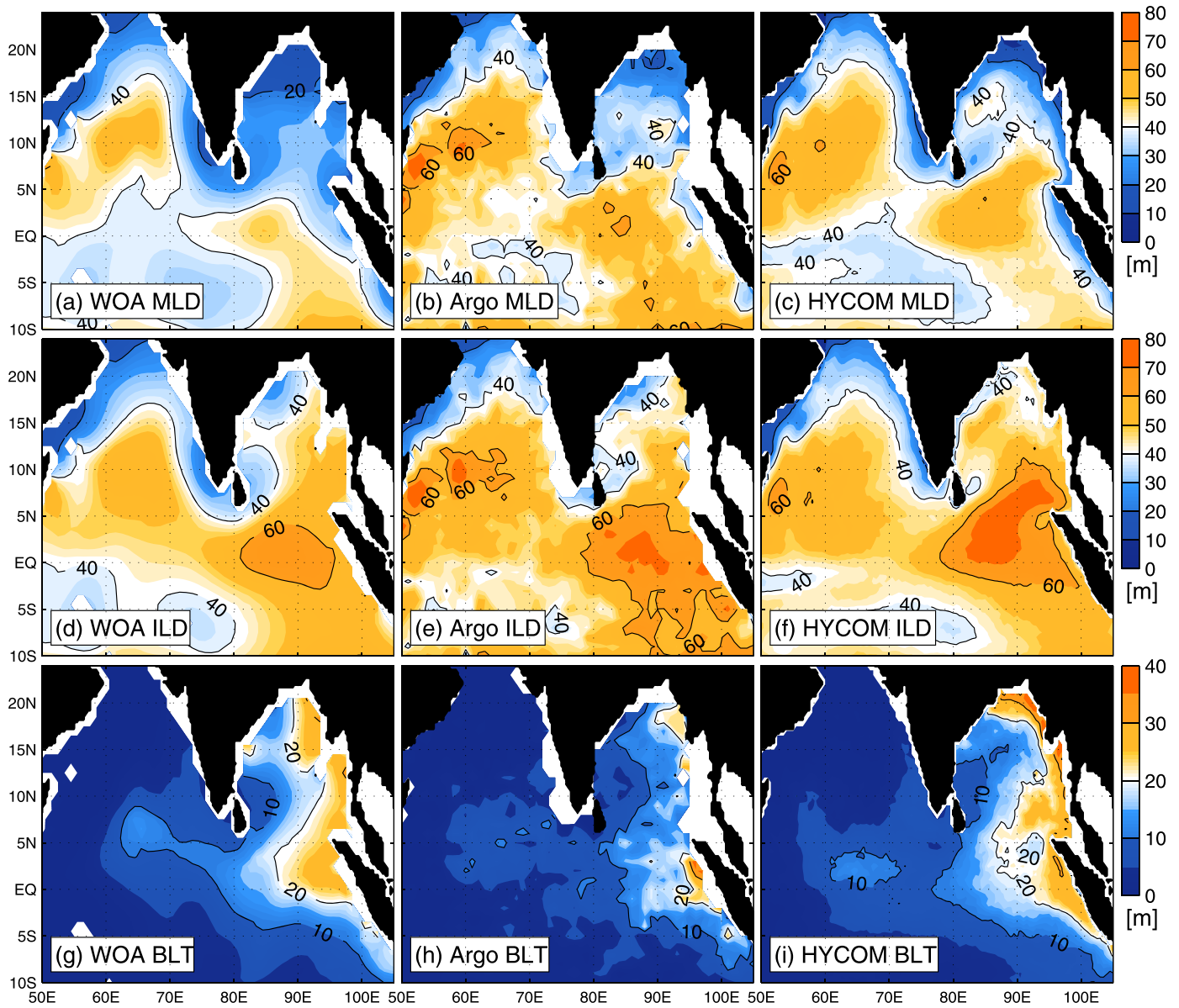

Figure 3. Climatologic MLD for May–October based on (a) WOA13 data, (b) Argo data of 2005–2014, and (c) HYCOM MR output of 2005–2014. Figures 3d–3f are the same as Figures 3a–3c but for ILD, and Figures 3g–3i are for BLT.

their mismatch in time period, given that the WOA13 climatology is based on in situ observations over 1955–2012, while the other two are for 2005–2014. We therefore employed another gridded data set, the 1° × 1° monthly product based on Argo data of 2005–2012, constructed and distributed by the Asia Pacific Data-Research Center (APDRC) of the International Pacific Research Center (IPRC) [*Lebedev et al.*, 2007], which adopts the same standard depth levels as WOA13. The estimated MLD and ILD using this product are quite similar to those based on WOA13 (supporting information Figure S1), ruling out the impact of period mismatch. To test the robustness of the results, we also adopted the 0.2°C criterion for the computations of MLD, ILD, and BLT (supporting information Figure S2). The MLD and ILD are shallower by around 5 and 10 m, respectively, than those computed with the 0.5°C criterion. The spatial distributions and cross-data differences are however not sensitive to the change in criterion. It is therefore likely that estimates based on gridded data sets tend to underestimate the MLD and ILD over the tropical Indian Ocean, likely due to the nonlinearity in MLD and ILD computation as pointed out by *de Boyer Montégut et al.* [2004]. This is why estimates based on individual profile data are preferable [e.g., *de Boyer Montégut et al.*, 2004, 2007; *Keerthi*

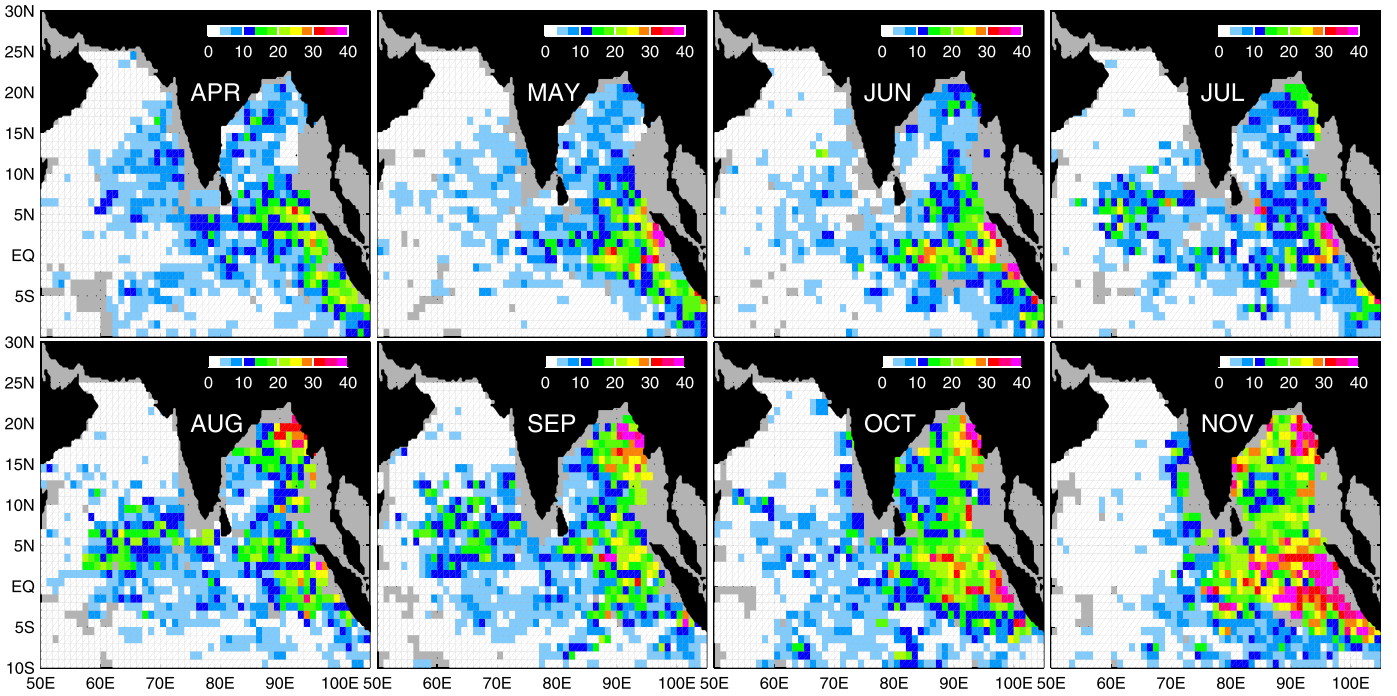

Figure 4. Monthly climatology of BLT (m) for April–November based on Argo profile data. Grids without enough data samples are masked gray.

et al., 2013]. In the BoB, the HYCOM-simulated BLT (Figure 3i) is larger than that in observation by several meters, mainly due to a deeper ILD (Figure 3f). Note that there are very few data available in the Andaman Sea (east of 95°E) and the coastal area along the BoB rim (Figure 1a). The simulated large BLTs in these areas are verified by existing observational studies [*Thadathil et al.*, 2007].

Figure 4 provides further check on the month-by-month evolution of BLT using Argo data. In the BoB the area of large BLT gradually enlarges during the ISM. In April–May, the premonsoon spring, the BLT is below 10 m in the BoB, with larger BLTs (∼20 m) occurring south of the bay near the Sumatra coast. During June–July, as the ISM develops, BLTs of 15–20 m appear first in the northeast corner of the bay. In August, the BLT reaches 20–30 m in the northern BoB, while in the southern bay it remains thinner than 10 m. Large BLT values are seen in most part of the bay by the decaying stage of the ISM (September–October) and continue to grow during the postmonsoon period (November). One exceptional area is the southwestern BoB (west of 85°E), where BLT is thinner than 10 m throughout the ISM. Comparing with the Arabian Sea and the western-to-central equatorial Indian basin, the BoB is a region of large BLT during the ISM period and ideal for investigating the role of barrier layer in the MISO. Our analyses below are therefore focused on the BoB interior region (85°E–95°E) where the mean BLT is large and Argo data sampling is sufficient.

Due to the dramatic meridional differences in MLD, ILD, and BLT in the BoB, we separately examine the seasonal variations for the northern BoB (NBoB; 14°N–21°N) and southern BoB (SBoB; 7°N–14°N) regions (Figure 5). The NBoB is characterized by a relatively shallower MLD (dashed curves in Figure 5a), which gradually deepens from 18 m in April to ∼35 m in July due to the strengthening monsoonal winds, and then rebounds to ∼20 m in September–October owing to the restratification by surface freshening (salinity showed in color shading) and the decaying monsoonal winds. The ILD, which is 10 m deeper than MLD in April–May, first follows the MLD deepening and departs from MLD afterward by staying around 45–50 m during July–October. The BLT exhibits a monotonic increase during the ISM, from 10 m in May–June to 30 m in September. These seasonal variations are realistically reproduced by the MR simulation of HYCOM (dashed curves). The simulated BLT tends to be larger by several meters during May–July, owing to the slightly shallower MLD and deeper ILD. The BLT based on WOA13 climatology (red) is also plotted, and it shows a better agreement with HYCOM. In the SBoB (Figure 5b), the MLD and ILD exhibit in-phase variations during the ISM, both of which deepen from May to September and shoal in October. The BLT shows a slight increase from 10 m in May–July to 15 m in October. These variations are also well simulated by

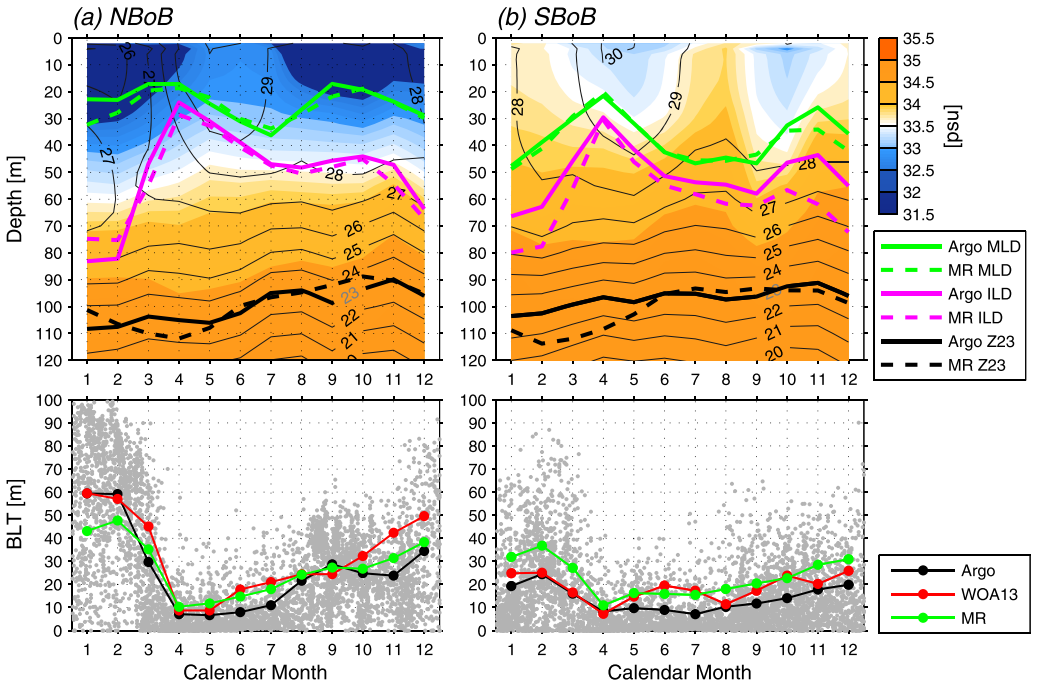

Figure 5. Seasonal evolution in the (a) NBoB (85°E–95°E, 14°N–21°N) and (b) SBoB (85°E–95°E, 7°N–14°N). The top figures show the depth-time plots of monthly climatological salinity (color shading; in psu) and temperature (contours; in °C) based on Argo profile data. The green, pink, and black thick curves denote MLD, ILD, and the 23°C isotherm (Z23; as a proxy of the thermocline depth), respectively, from Argo data (solid) and HYCOM MR (dashed). The bottom figures compare the monthly mean BLT from Argo profile data (black), WOA13 climatology (red), and HYCOM MR (green). The gray dots show the BLT samples from individual Argo profiles.

HYCOM. Albeit with a nearly perfect simulation of MLD, the simulated BLT is larger than observation by about 5–8 m, due to the deeper ILD. The BLT from WOA13 again agrees better with HYCOM. Although HYCOM and WOA13 overestimate the mean BLT, seasonal variations of BLT are consistent among the three data sets. Interestingly, in both the NBoB and SBoB the seasonal ILD variation during the ISM opposes that of the thermocline depth, which can be represented by the 23°C isotherm (Z23; black curve): ILD deepens, while the thermocline shoals. This relationship is also captured by HYCOM. The variations of ILD and thermocline depth are likely controlled by different mechanisms during the ISM season. While the thermocline variation is primarily baroclinic wave responses to wind forcing [e.g., *Han and Webster*, 2002; *Rao et al*., 2010; *Girishkumar et al*., 2013], the ILD, as will be shown in section 4, is sensitive to surface heat flux, which affects ILD through mixing.

3.2. Intraseasonal Variability During MISO Events

We further assess the intraseasonal variations induced by MISOs. Unless otherwise noted, "intraseasonal anomaly" in this study is obtained through first removing the seasonal cycle and then applying a 20–90 day band-pass Lanczos filter. We use the intraseasonal anomaly of TRMM precipitation averaged in the BoB box (85°E–95°E, 7°N–21°N) for the selection of MISO events (Figure 6a). Precipitation maxima exceeding one standard deviation (STD) during May–October are identified as the convection peaks of MISOs (asterisks) and taken as the "zero" day of the MISO composite. Under this criterion, there are 48 events that occurred during 2002–2015, among which 35 occurred during the Argo observation period of 2005–2015 (red asterisks). We search Argo data samples located between 85°E and 95°E and within 30 days before and after the MISO convection peaks (Figure 6b). The profile number generally increases with latitude. For most of the 3 day $\times$ 1° latitude grids within the BoB (north of 7°N) 10 profiles are available. By averaging these data samples, we obtain the time-latitude plots of MLD, ILD, and BLT anomalies of the composite MISO (Figures 7a–7c). For the MLD, ILD, and BLT anomalies here, the mean seasonal cycle is removed. The positive precipitation anomaly, characterizing the MISO active phase, moves from the equator to the BoB and strengthened to $>$10 mm d^{-1} between 15°N and 19°N. Prior and subsequent to the active phase, there are negative precipitation anomalies, characterizing the break phase of the MISO. Variations of MLD and ILD are

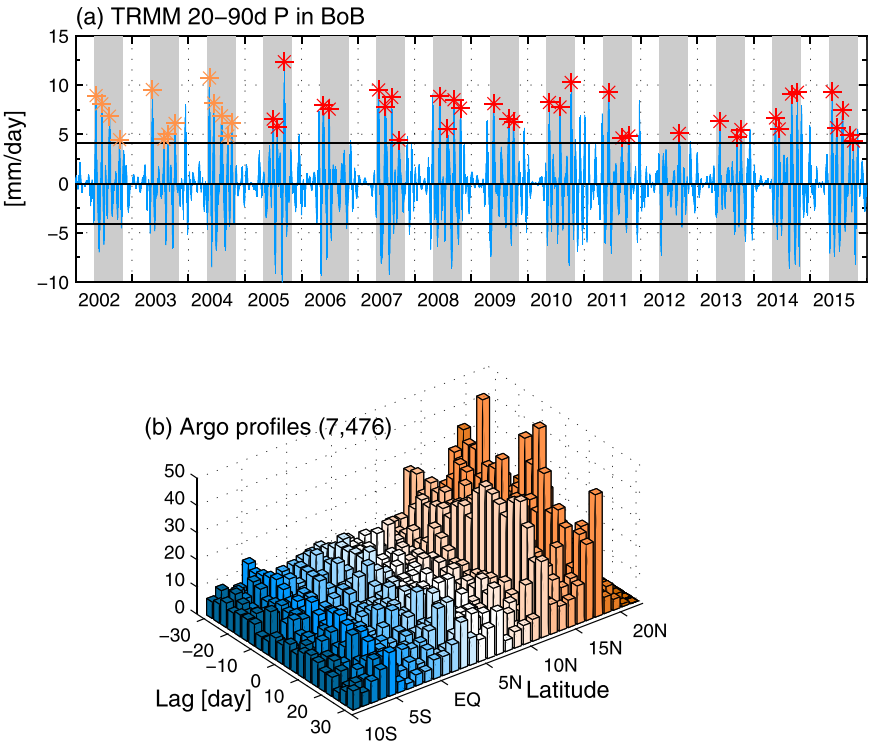

Figure 6. (a) 20–90 day TRMM precipitation in the BoB box. Orange and red asterisks denote the maxima exceeding the STD range (black lines) occurred in 2002–2004 and 2005–2015. (b) Distribution of Argo profiles between 85°E and 95°E with respect to time lag (3 day interval) and latitude (1° interval) for the composite MISO.

generally similar, showing negative anomalies before and positive anomalies after the MISO convection, indicating a deepening during the passage of the MISO. It is discernible that the deepening of ILD is larger than MLD, as indicated by the larger positive ILD anomaly after +5 day (Figure 7b).

In comparison, the BLT anomaly pattern is much noisier (Figure 7c). The present Argo data sampling is likely not sufficient to average out the noises of event-by-event variability and ocean eddies. Nevertheless, it is still discernible that more negative BLT anomalies (thin BLT) occur before and during the active phase, and more positive BLT anomalies (thick BLT) are seen after the active phase, indicative of a thickening of the barrier layer by several meters throughout the MISO event. The variability patterns in HYCOM MR are much better organized (Figures 7d–7f). A clear deepening tendency is seen in MLD and ILD during the active phase of the MISO, with the ILD showing larger anomalies in magnitude. The simulated BLT shows negative anomalies before and during the MISO active phase and positive anomalies during the postconvection break phase, confirming the variations seen in the Argo composite map. In HYCOM, the BLT variations are apparently much weaker than those of MLD and ILD.

Box averaging is able to better damp the noises by involving more data samples (Figure 8). The in-phase relationship between MLD and ILD is clearly displayed. Both of them are shallowest when the convection begins to develop and deepest by the end of the active phase. In the NBoB the gap between MLD and ILD is slightly enlarged due to the larger deepening rate of ILD, which leads to a ∼5 m increase in BLT throughout the MISO event (Figure 8a). Variations from Argo and HYCOM agree well. HYCOM does not replicate the abrupt shallowing of ILD at −5 day as shown in Argo. This phenomenon is however likely induced by sampling error instead of a MISO-forced signal. In the southern BoB the variations of MLD and ILD are not only in phase but also with close amplitudes (Figure 8b). As a result, the composite BLT is maintained at ∼10 m throughout the MISO both in Argo observation and HYCOM simulation. In HYCOM, the BLT is slightly increased after +5 day by about 2 m. These BLT variations are however insignificant compared to the large error range, and their amplitudes are also too small compared to the vertical resolution of HYCOM and Argo observation. Strong seasonal and interannual variations in the background state are seen in Figures 2 and 4, and event-by-event variability is also large (figure not shown). For the Argo composite, spatial sampling of

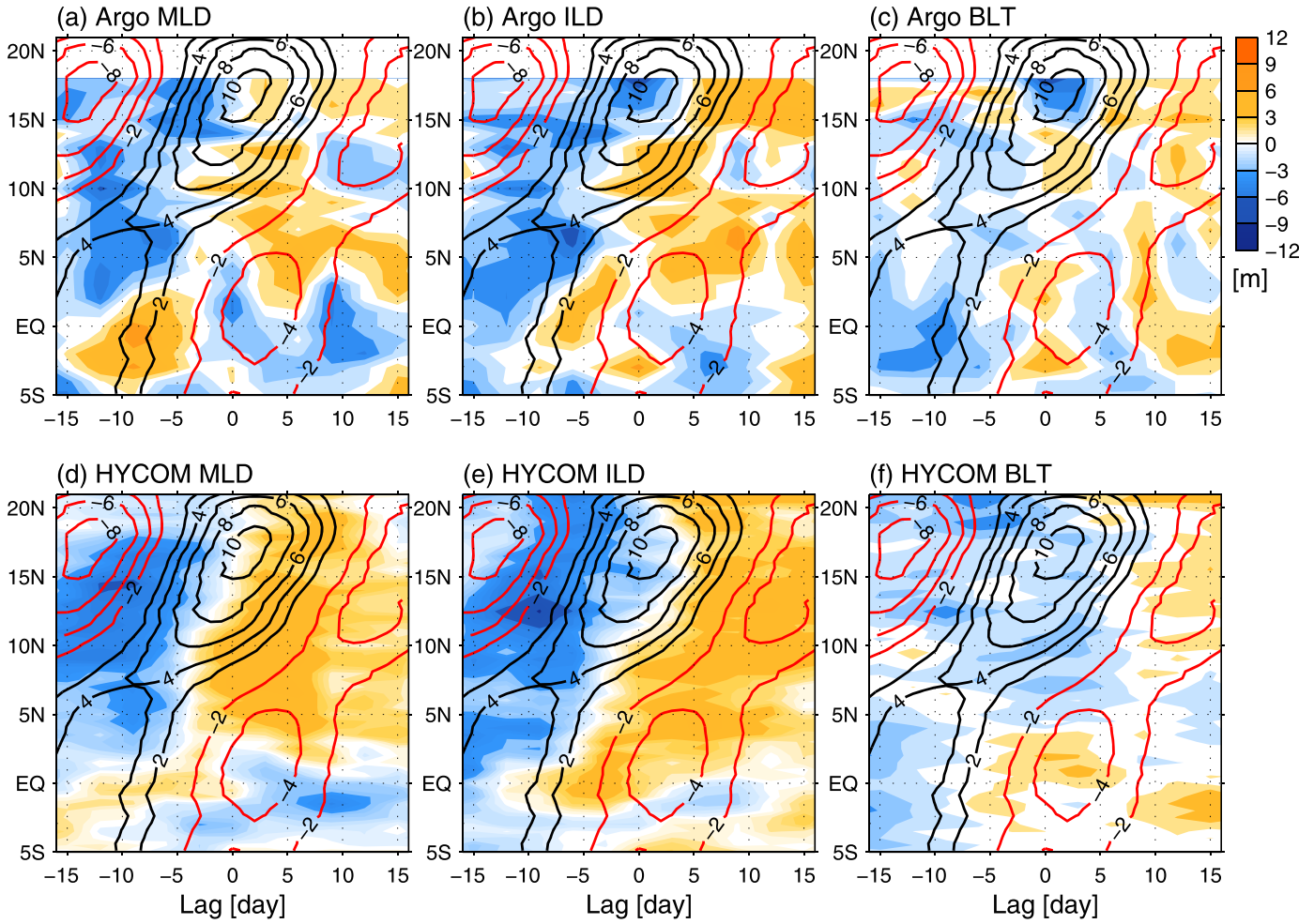

Figure 7. Time-latitude plots of (a) MLD, (b) ILD, and (c) BLT anomalies averaged over 85°E–95°E in the composite MISO (m) based on Argo profile data, which are smoothed with a three-latitude running mean. Figures 7d–7f are the same as Figures 7a–7c, but from HYCOM MR. Black and red contours denote the positive and negative anomalies of the 20–90 day TRMM precipitation (mm d^{-1}). Composites are based on the 30 MISO events during 2005–2014.

data profiles is also a major source of error. Again variation of Z23 again has the opposite sign of ILD, as in the case of seasonal variation shown in Figure 5. The MISO induces a shoaling of the thermocline by ~8 m in both Argo observation and HYCOM, which will be further discussed in section 4.2. Composite analysis is also performed for the MLD, ILD, and BLT computed with the 0.2°C criterion (supporting information Figure S3). These composites show similar variability features to Figure 8 during the MISO event.

Given the low signal-to-noise ratio, the BLT variations described here require further confirmation from another independent data source. We conduct a similar composite analysis with the data of the three RAMA buoys within the bay (Figure 9). In general, the composite variations observed by RAMA are quite consistent with those from HYCOM, with in-phase deepening of MLD and ILD, shoaling of Z23, and small changes in BLT. BLT is increased by ~5 m at B1 (15°N) and ~8 m at B2 (12°N), magnitudes close to HYCOM simulation. Note that the RAMA buoy did not observe the abrupt ILD shallowing on −5 day in Argo composite (Figure 8a). The BLT increase is not even visible at B3 (8°N), confirming the larger variation in NBoB than in SBoB. The weak changes of the composite BLT is in an apparent contrast to the original BLT time series (Figure 2d) in which intraseasonal fluctuations of 10–20 m are seen. In addition, the MLD and ILD variations in Figure 2d are also dramatically larger than the composite changes. A similar phenomenon was reported by *Drushka et al.* [2014]. The authors found very weak composite intraseasonal BLT variability in the eastern equatorial Indian Ocean. To gain insight into of this issue, a comprehensive investigation for the underlying mechanisms is required.

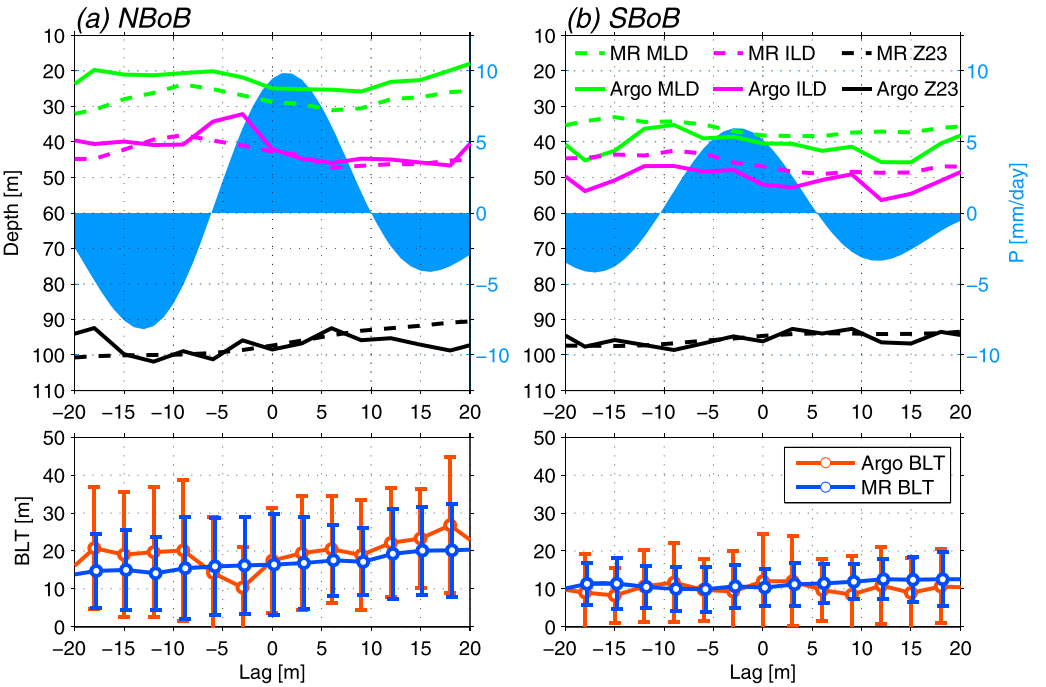

Figure 8. MISO composites in the (a) NBoB and (b) SBoB regions. The top figure shows the 20–90 day TRMM precipitation (blue shading) and MLD (green), ILD (pink), and Z23 (black) from Argo data (solid) and HYCOM MR (dashed). The bottom figure shows the BLT (doted curve) and its STD (error bar) from Argo data (red) and HYCOM MR (blue). Composites are based on the 30 MISO events during 2005–2014.

4. Mechanisms of Intraseasonal Variability

4.1. HYCOM Experiments

Oceanic variability at intraseasonal timescale can be caused by various processes. To evaluate their relative importance, five parallel HYCOM simulations are performed for the 2000–2014 period, starting from the

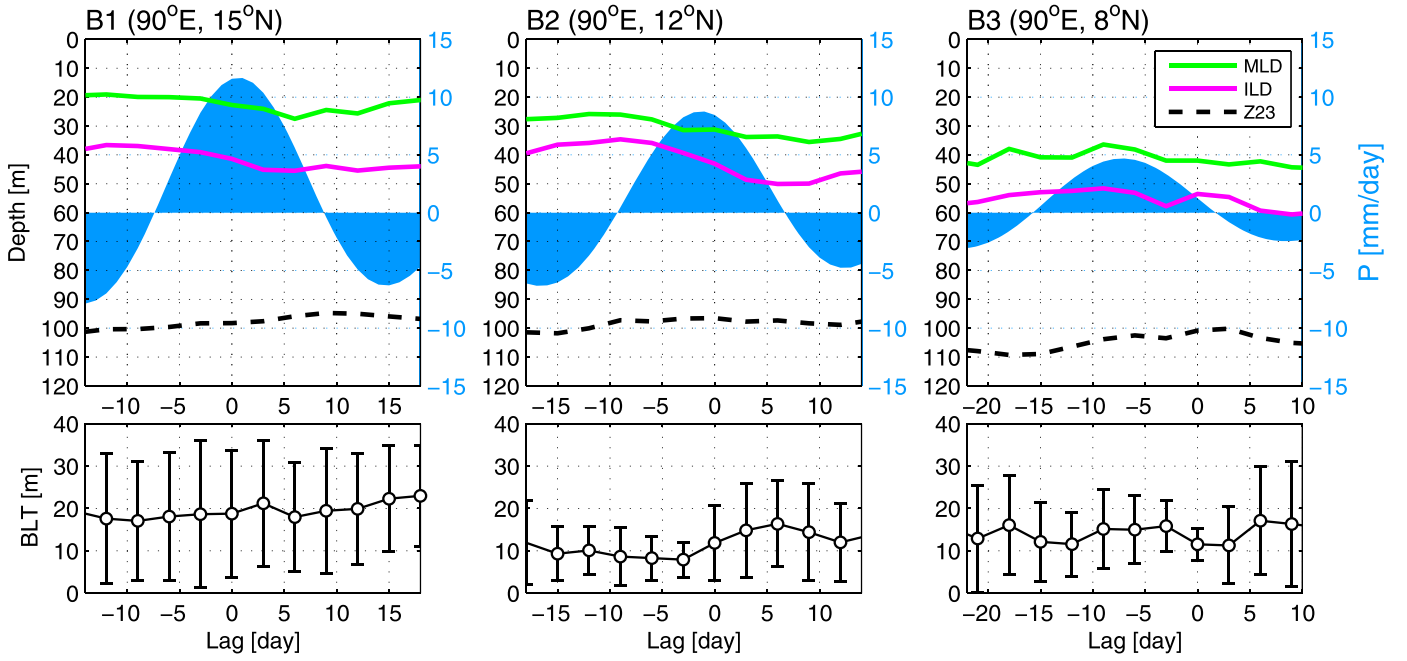

Figure 9. Top figures show the MISO composites of 20–90 day TRMM precipitation (blue shading), MLD (green), ILD (pink), and Z23 (black dashed) from RAMA buoys B1, B2, and B3, and the bottom figures show the corresponding composite BLT and its STD. As for Figures 7 and 8, composites are conducted relative to the average 20–90 day precipitation of the BoB box and based on the 21 MISO events during 2008–2014.

same initial condition as MR. In the NoISO run, intraseasonal variability in the atmospheric forcing fields are removed with a 105 day low-pass Lanczos filter, so that the ocean intraseasonal variability arises only from the ocean internal instabilities [*Jochum and Murtugudde*, 2005]. The solution difference, MR – NoISO, therefore represents the overall forcing effect of the MISO in boreal summer. The cloud-controlled surface SWR change is an important driver for the ocean temperature changes at intraseasonal timescale [e.g., *Sengupta et al*., 2001; *Duncan and Han*, 2009; *Vialard et al*., 2012]. In the NoSWR experiment, only SWR is 105 day low-pass filtered, so that the effect of intraseasonal SWR is removed. The difference, MR – NoSWR, represents the SWR effect of the MISO on the ocean. Similarly, in the NoTAU experiment, wind stress is 105 day low-passed filtered, and therefore MR – NoTAU represents the effect of wind stress-driven ocean processes, such as horizontal advection, upwelling, and turbulent mixing. This effect is termed as the "wind stress effect" hereafter. In the NoWND experiment, both wind stress and wind speed are low-pass filtered. Therefore, NoTAU – NoWND provides an estimate for the wind speed effect on the ocean through evaporation and turbulent heat flux Q_T (hereafter "wind speed effect"). Lastly, in the NoP experiment precipitation is low-pass filtered, and the precipitation effect is represented by MR – NoP. The 3 day mean outputs of the five experiments for 2002–2014 are used for analysis.

4.2. Processes

We first assess the intraseasonal variability arising from ocean internal instabilities, by comparing HYCOM simulations of MR and NoISO in the 20–90 day STD (Figure 10). Intraseasonal variations of MLD, ILD, and BLT are stronger (STD $>$ 10 m) in the eastern BoB and weaker (6–8 m) in the western BoB. Variations in the eastern bay are connected to stronger signals (12–16 m) in the eastern equatorial Indian basin. Interestingly, the STD maps from NoISO (Figures 10d–10f) are close to those of MR (Figures 10a–10c), with similar spatial distributions and comparable magnitudes. The difference between the STDs of MR and NoISO (Figures 10g–10i) shows 3–6 m signals in the far northern part of the bay and in the western and eastern equatorial basin, but in most part of the bay this effect is close to zero. This suggests that the large equatorial wind anomalies of the ISOs can significantly enhance MLD and ILD variability. In the BoB region, however, the atmospheric forcing cannot significantly enhance the pointwise intraseasonal variability of ocean stratification. In NoISO there is no intraseasonal atmospheric forcing, and therefore variability of ocean stratification arises predominantly from ocean internal instabilities, such as the pronounced eddy variability there [e.g., *Gopalan et al*., 2000; *Kurien et al*., 2010; *Chen et al*., 2012; *Cheng et al*., 2013]. This provides a plausible explanation for why the RAMA buoy records show strong intraseasonal variations (Figure 2), whereas MISO composite variations seen in Figures 7–9 are weak. This finding is consistent with recent observational studies showing that mesoscale and submesoscale eddies in the BoB are a major driver of intraseasonal variations in near-surface salinity and stratification [*Parampil et al*., 2010; *Sengupta et al*., 2016].

A large portion of the internally generated variability manifests as mesoscale signals, while the MISO-forced variations tend to have basin-scale structures. We further examine the area-averaged intraseasonal variability for the NBoB and SBoB regions (supporting information Figure S4), in which the mesoscale variability has been averaged out. In the NBoB, the STDs of the 20–90 day MLD from MR and NoISO are 5.2 and 3.4 m, while those of the 20–90 day ILD are 5.7 and 4.5 m, respectively. Similarly, in the SBoB, MR and NoISO have MLD STDs of 4.0 and 3.0 m and ILD STDs of 5.3 and 3.8 m, respectively. The BLT STDs from the two experiments are very close. Although still weaker than ocean internal variability, MISOs contribute to $\sim$20–40% of the large-scale MLD and ILD variations in the BoB. The weak effect of MISOs on BLT is likely owing to the in-phase relationship between MLD and ILD anomalies (Figure 8).

To gain insights into the processes through which MISOs affects the ocean stratification, hereafter we focus on the composite MISO variability in the BoB, in which MISO-forced variability is highlighted. This composite is performed with intraseasonal anomalies of ocean and atmospheric variables (seasonal cycle removed and 20–90 day band-pass filtered) except for MLD, ILD, and BLT anomalies for which we only removed their mean seasonal cycles. Figure 11a shows the composite intraseasonal anomalies of surface atmospheric fields in the NBoB. The precipitation minimum, representing the break phase of the MISO, occurs at -12 day and is accompanied by weak winds, enhanced downward SWR, and positive downward Q_T anomaly (indicating reduced cooling for the ocean due to weak winds). In HYCOM there is net surface heat flux Q_{net} in model output, and the downward Q_T can be estimated simply as $Q_T = Q_{net}$ – SWR – LWR. As the MISO convection develops from -12 day to $+2$ day with increasing rainfall, the convective cloud blocks SWR, and the strengthening surface wind speed leads to negative Q_T anomaly (enhanced cooling for the ocean).

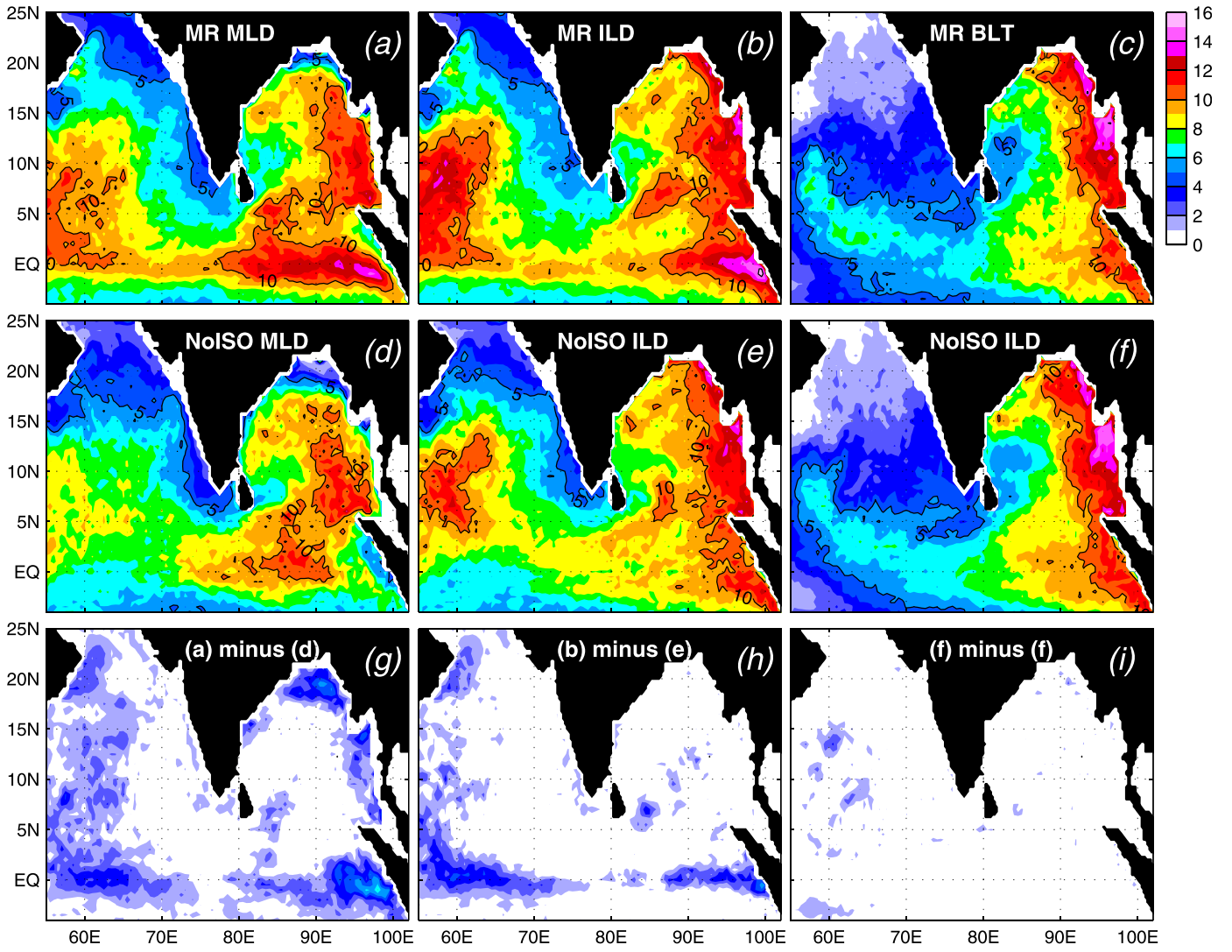

Figure 10. STDs of the 20–90 day band-pass filtered (a) MLD, (b) ILD, and (c) BLT during May–October of 2002–2014 from HYCOM MR experiment. Figures 10d–10f are the same as Figures 10a–10c but from NoISO experiment.

Note that LWR anomaly is much smaller in magnitude than SWR and Q_T and out of phase with them, so that its influence on the ocean is quite small. Alternatively, SWR and Q_T anomalies are comparably large (20–30 W m^{-2}) and in phase, they together lead to a warming of 0.1–0.4°C in the upper 30 m during the break phase of MISO and a strong cooling during the active phase (Figure 11b). Anomalies in ocean salinity are as large as 0.2 psu. It is somewhat surprising that high salinities occur roughly with precipitation peak, which challenges our conventional understanding for their relationship. If salinity change is dominated by precipitation, the two should exhibit a quadrature phase relationship, with enhanced (reduced) precipitation leading negative (positive) salinity anomaly.

To confirm the simulated salinity variability, we performed a similar composite with Aquarius SSS data, which also showed a roughly in-phase relationship with TRMM precipitation in the NBoB region (gray curve in Figure 11c), although its anomaly magnitude is larger by ~30% than HYCOM MR (black). The weaker SSS anomaly in HYCOM may be attributed to three reasons. First, as discussed in previous studies [e.g., *Li et al.*, 2015; *Song et al.*, 2015], satellite SSS represents the skin-layer salinity and tends to have larger variability than bulk salinity from in situ observation and model simulation; second, our HYCOM simulations, using monthly river discharge, do not resolve the intraseasonal variability of river freshwater input which could be influential in the NBoB area; third, the vertical resolution of HYCOM in the near-surface layer is still not sufficiently fine to fully resolve the sharp salinity stratification near the northern boundary of the bay [e.g.,

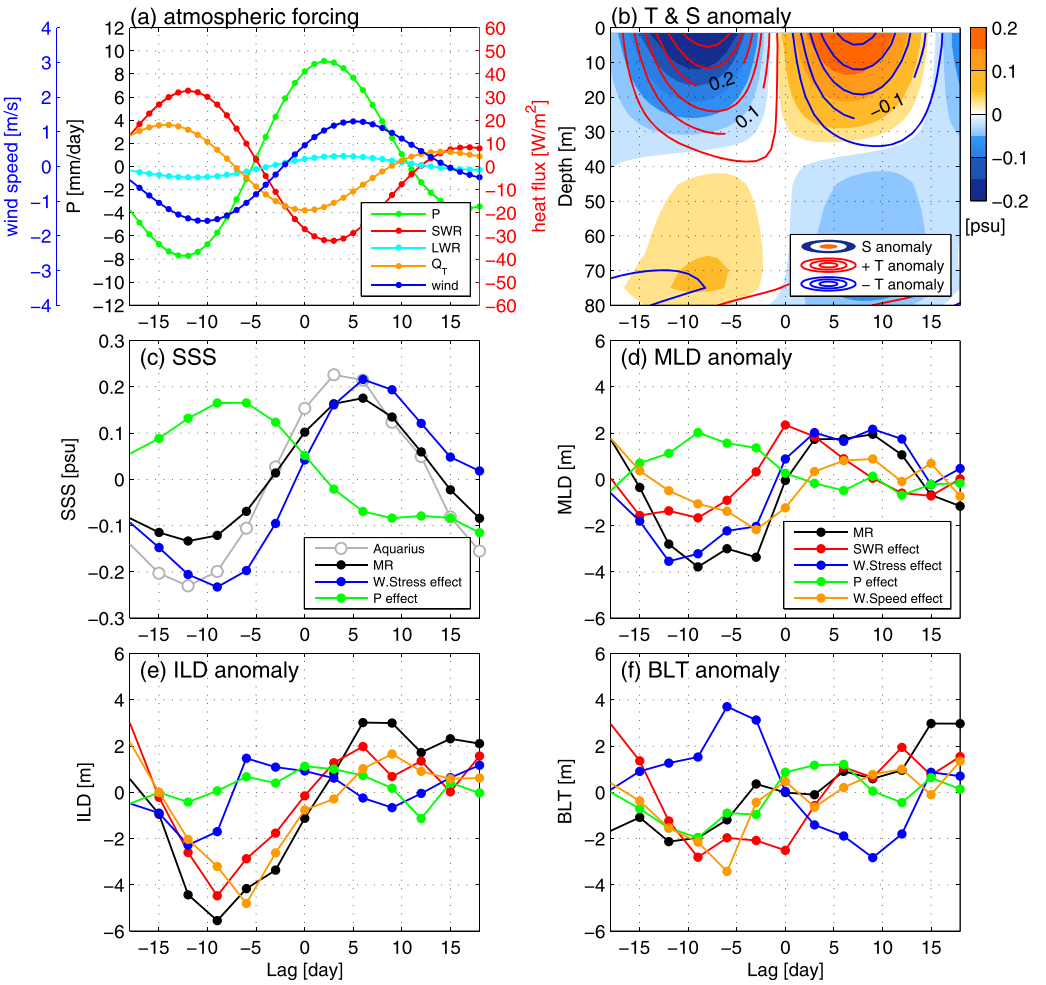

Figure 11. MISO composite for the NBoB region: (a) intraseasonal surface fluxes, including TRMM precipitation (green), observed wind speed (blue), SWR (red), and LWR (cyan) from CERES, and turbulent heat flux Q_T (brown) from MR; (b) intraseasonal temperature (°C) and salinity anomaly profiles in MR; (c) intraseasonal SSS from Aquarius data (gray), MR (black), MR – NoTAU (blue; wind stress effect), and MR – NoP (green; precipitation effect); (d) MLD, (e) ILD, and (f) BLT anomalies from MR (black), MR – SWR (red; SWR effect), MR – NoTAU (blue), MR – NoP (green), and NoTAU – NoWND (brown; wind speed effect). Composites are based on the 43 MISO events during 2002–2014, except for the Aquarius SSS which is based on 13 events during 2011–2015.

Sengupta et al., 2016]. The incoherent intraseasonal variability of precipitation and SSS were also observed in the eastern Indian Ocean and western Pacific Ocean [*Guan et al*., 2014]. Data analysis and model experiments demonstrate that these large-scale intraseasonal SSS anomalies are produced by ocean current advection driven by intraseasonal winds and therefore do not follow the freshwater flux changes [*Matthews et al*., 2010; *Li et al*., 2015; *Li and Han*, 2016].

The model results demonstrate that in the NBoB, winds rather than precipitation drive the SSS anomalies during MISO events. The wind stress effect, as measured by the MR – NoTAU solution, produces strong SSS anomalies (blue curve in Figure 11c) that basically dominate the total SSS. By contrast, the precipitation effect on SSS (green), measured by MR – NoP, is smaller and roughly out of phase with the total and wind stress-driven SSS anomalies. Note that the SSS anomaly produced by precipitation indeed lags precipitation anomaly by several days. Since wind stress-driven SSS anomaly is larger in magnitude, it overcomes the precipitation effect and dominates the total SSS anomaly.

The wind stress effect on SSS can be understood by considering the horizontal salinity advection of anomalous surface currents (Figure 12). For instance, the wind stress anomaly pattern during the preconvection break phase (Figure 12a), implying a weakening of the southwesterly monsoon, induces prevailing westward surface current anomalies in the BoB (Figure 12b), probably in forms of both Ekman and geostrophic

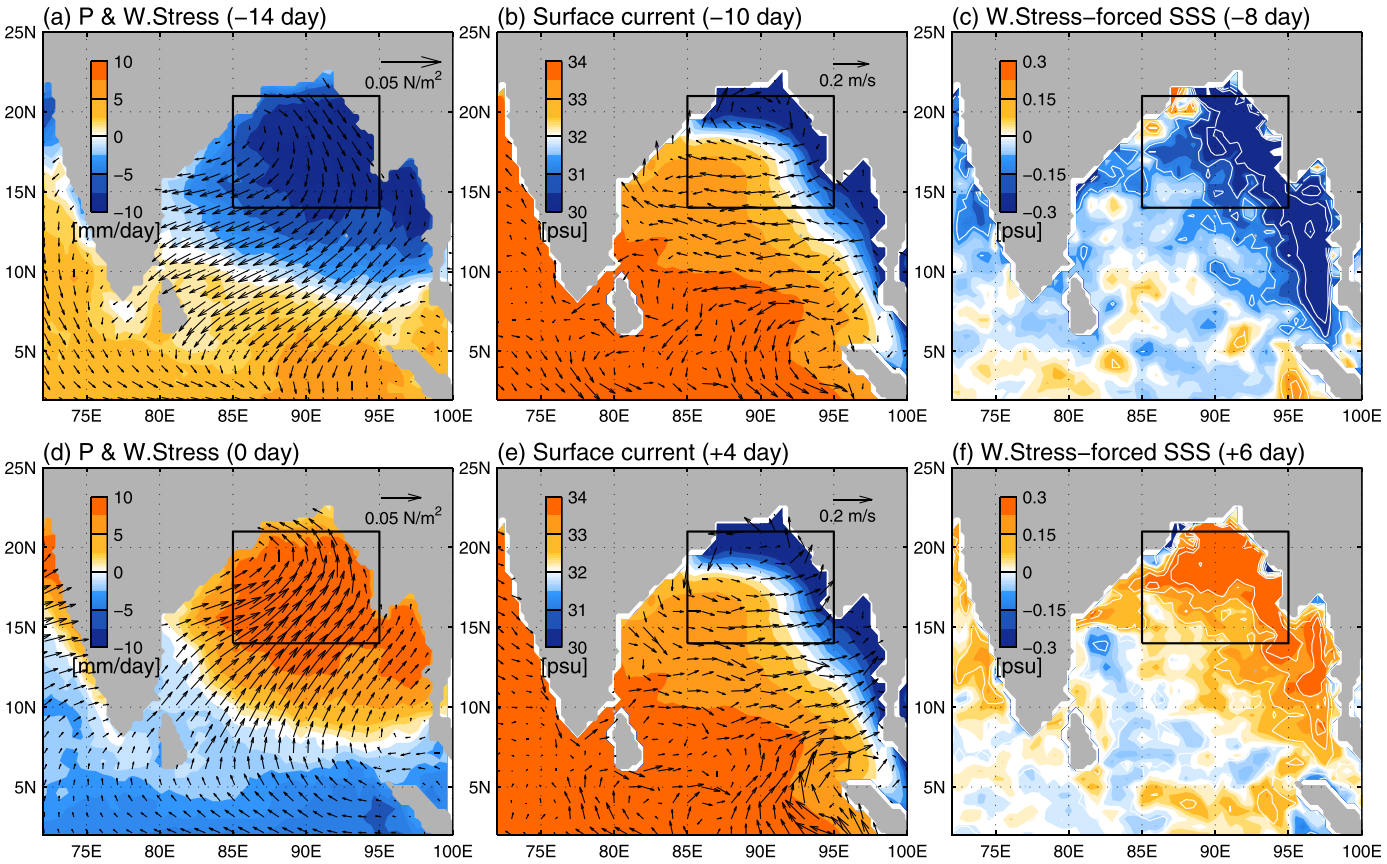

Figure 12. Intraseasonal anomalies of the MISO composite for the NBoB region: (a) TRMM precipitation (color shading) and observed wind stress (vectors) at −14 day, (b) surface current in MR – NoTAU at −10 day (vectors), and (c) SSS in MR – NoTAU at −8 day. Figures 12d–12f are the same as Figures 12a–12c but at 0 day, +4 day, and +6 day, respectively. The color shading in Figures 12b and 12e is climatologic mean SSS in MR for the ISM season.

currents. These anomalous currents transport the fresh water from the coastal area along the northeast boundary, which is mainly formed by the discharge of Ganges-Brahmaputra and the Irrawaddy, to the bay interior and leads to a basin-wide surface freshening (Figure 12c). The opposite scenario occurs during and after the convection peak. Strengthening of the southwesterly monsoon (Figure 12d) induces eastward surface currents (Figure 2e), which carries the saltier water in the southwest bay eastward and leads to a basin-wide salinity rise (Figure 2f). Note that in response to wind stress forcing, an anticyclonic gyre is formed in the NBoB region in the preconvection break phase (Figure 12b), while a cyclonic gyre is seen there after the convection peak (Figure 12c). This explains the thermocline shoaling during the MISO (recall Figures 8 and 9) and confirms the notion that thermocline depth variations in the BoB are primarily baroclinic wave responses to wind forcing [*Rao et al.*, 2010; *Girishkumar et al.*, 2013].

The multivariate atmospheric forcing of the MISO has a complex effect on ocean stratification. Figure 11d shows the composite MLD anomaly induced by different effects. The ∼6 m increase of MLD from −9 to +9 day in MR is primarily driven by wind stress effect (MR – NoTAU) which induces a ∼5.5 m increase. Wind stress controls ocean near-surface turbulent mixing by stirring. Weak (strong) wind stress at the break (active) phase (Figure 11a) fuels less (more) kinetic energy for ocean turbulent mixing near the sea surface, and leads to a shallow (deep) MLD. Another effect of wind stress is through ocean salinity. Wind stress-produced surface freshening (salinity rise) at the break (active) phase, as shown in Figure 11c, is fundamental for maintaining the shallow (deep) MLD. We are however unable to separate the two effects of wind stress and evaluate their relative importance. Surface buoyancy forcing by heat fluxes also has significant contribution to MLD change. During the preevent break phase, surface warming by SWR (red; measured by MR – NoSWR) and wind speed-controlled Q_T (brown; measured by NoTAU – NoWND) reduce the surface water density and thus entrainment, helping to maintain the shallow MLD. By contrast, during the active phase their strong cooling effect deepens the MLD. The contribution of precipitation to MLD change is

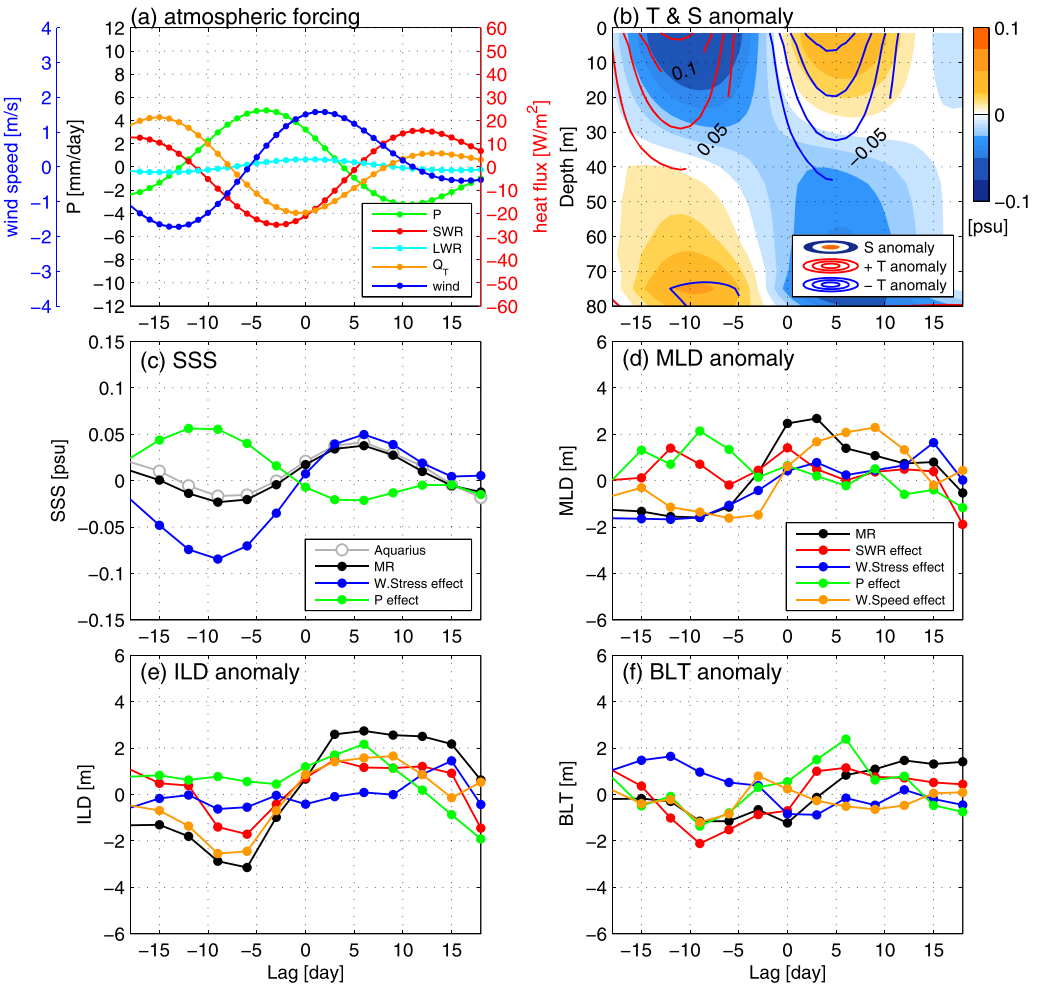

Figure 13. The same as Figure 11 but for the SBoB region.

negative, which can be understood by considering its impact on SSS. The increasing rainfall during the transition from break to active phase leads to surface freshening (precipitation effect on SSS in Figure 11c), stronger stratification and weakened entrainment, favoring the MLD shoaling. The contributions of SWR and Q_T to the MLD increase from -9 to $+9$ day are 1.7 and 1.8 m, respectively, much smaller than wind stress effect.

Unlike MLD or the thermocline depth, the ILD change is primarily controlled by heat fluxes, with SWR and Q_T having roughly equal contributions (Figure 11e). Wind stress also contributes to the ILD deepening, and this effect is smaller than that due to heat flux. Precipitation has no significant effect on ILD. Since different processes control the MLD and ILD changes, the cause for BLT variation is rather complicated (Figure 11f). The two types of heat fluxes, SWR and Q_T, contribute to the BLT expansion, due to their large impact on ILD deepening. Precipitation of the MISO convection also helps in the growth of BLT by freshening the sea surface and shoaling the MLD. These effects are however partly offset by wind stress, which induces a quick deepening of the MLD and thereby reduces the BLT. This offsetting effect is likely responsible for the weak BLT change during the MISO.

In comparison, the composite variations in the SBoB are weaker (Figure 13a). Anomalies of precipitation and SWR during the active phase are $+24$ mm d^{-1} and -25 W m^{-2} smaller in magnitude than the $+46$ mm d^{-1} and -33 W m^{-2} in the NBoB by ~40%. Interestingly, despite weaker convection and radiative flux, wind and Q_T anomalies are as large as those in the NBoB. Temperature and salinity anomaly structures (Figure 13b) are similar to those in the NBoB but with only half of the magnitudes. Again surface salinity changes are dominated by wind stress forcing, which overcomes the opposite effect by precipitation

(Figure 13c). Instead of the domination by wind stress, the MLD change in the SBoB is driven by both wind stress and wind speed-controlled Q_T (Figure 13d). On the other hand, the ILD deepening is mainly contributed by SWR and Q_T, with the Q_T effect being larger (Figure 13e). Note that the large ILD between 0 and +10 day also benefits from precipitation. This process is imposed through MLD. Enhanced rainfall leads to surface freshening and MLD shoaling (green curves in Figures 13c and 13d), which can further strengthen the surface cooling (Figure 13b) induced by heat fluxes and thereby contribute to the deep ILD. The BLT change in the SBoB is too weak to clarify the dominant driver, but an offset between wind stress effect and the others is clearly seen again (Figure 13f). Results in Figures 11 and 13 suggest that MISOs modulate the BoB stratification structure via a complex mechanism. Although the MLD and ILD show in-phase variations, they are in fact controlled by different processes. Wind stress dominates MLD change by affecting turbulent mixing and SSS, while heat fluxes, particularly SWR and wind speed-controlled Q_T, are the main drivers of ILD change. Meanwhile, wind stress effect on BLT is opposite to those of heat fluxes, and this offsetting is responsible for the limited BLT change during the MISO.

5. Summary and Discussion

The ISM during May–October brings a huge amount of freshwater flux into the BoB in forms of heavy rainfall and enhanced discharges of the major rivers such as the Ganges-Brahmaputra and the Irrawaddy. The freshwater flux gives rise to sharp near-surface salinity stratification in the BoB, characterized by a shallower MLD and a thicker barrier layer than other areas of the Indian Ocean basin. The BoB also locates on the pathway of the northward propagating MISO, i.e., the dominant variability mode of the ISM at intraseasonal timescale. The roles played by the MLD and BLT of the BoB in the MISO are however rarely investigated. As the first part of the investigation, this paper provides a comprehensive investigation for the intraseasonal variability of MLD and BLT, exploring the spatial-temporal characteristics and driving mechanisms, using the recently accumulated in situ observations and HYCOM simulations forced with satellite atmospheric data sets.

During the ISM, the BoB has a shallow MLD of ~20 m in the north and a deeper one (30–40 m) in the south, and by contrast its mean barrier layer is thicker in the north (20–30 m) and thinner in the south (10–15 m). Intraseasonal variability of MLD and BLT rides over a strong seasonal cycle, in which the MLD shows a shallow-deep-shallow evolution during the ISM and meanwhile the BLT monotonically increases from ~10 m in May to 20–40 m in September–October. Composite analysis for the MISO with Argo data and HYCOM result reveals that during the passage of the MISO both MLD and ILD are deepened by 8–15 m. Due to this in-phase relationship between MLD and ILD, the composite BLT change is rather small. In the northern bay (14°N–21°N) the BLT is increased by about 5 m by the MISO, owing to a larger deepening of ILD than MLD. In the southern bay (7°N–14°N) the composite BLT is increased by only ~2 m. These changes are however within the error range of Argo data sampling and Argo floats' measurement resolution. The composite BLT change is also small compared with the event-by-event spread in HYCOM simulation. These results are confirmed by a composite analysis with RAMA buoy measurements.

Since the HYCOM is able to realistically simulate the observed mean state, seasonal cycle, and MISO-induced intraseasonal variability of the ocean stratification, we further explore the underlying processes with HYCOM experiments. A comparison between MR and NoISO suggests that in the BoB the pointwise intraseasonal variations of MLD, ILD, and BLT are predominantly signatures of ocean internal instabilities, such as the pronounced mesoscale eddies in this region. This explains the much stronger fluctuations in the records of RAMA buoy measurements than in MISO composites. Ocean internal instability also has larger impact on the large-scale (box-averaged) ocean salinity stratification variability in the BoB than MISO forcing, with the latter contributing by 20–40% to the total intraseasonal variability of MLD and ILD.

Further analysis reveals that the in-phase variations of MLD and ILD are induced by different processes. The MLD deepening is primarily driven by wind stress forcing via enhancing turbulent mixing and raising surface salinity, and it is secondarily contributed by surface heat fluxes through surface cooling. The heat flux forcing, specifically reduced shortwave radiation and enhanced upward Q_T, is the main cause for the ILD deepening. The effects of wind stress and precipitation on ILD are relatively small. The BLT change is therefore produced under the mixed effect of different processes. The surface cooling by heat fluxes acts to enlarge BLT by deepening the ILD. This change is supported by precipitation that shoals the MLD through

surface freshening (as indicated by the SSS anomaly from MR – NoP solution in Figures 11c and 13c). However, this combined effort is greatly offset by wind stress effect, which deepens the MLD and thereby reduces the BLT. As a result, the BLT change is rather limited.

The ILD change is opposite to the thermocline depth change which shows a shoaling during the MISO. This is not in line with our conventional understanding that the ILD can be considered as the top of the thermocline, and its variability should be in phase with the thermocline fluctuation. For example, in the BoB region, intraseasonal ILD variations observed at RAMA buoys largely follows the thermocline depth [*Girishkumar et al*., 2011]. This discrepancy can be reconciled here. As indicated in our results, the pointwise intraseasonal variability of ILD, such as that observed by a moored buoy, is largely manifestations of mesoscale eddies or otherwise wind stress-forced baroclinic waves [e.g., *Girishkumar et al*., 2011]. In these adiabatic ocean processes, both the thermocline and ILD are modulated by vertical stretching of the upper-ocean water column, which leads to in-phase variations of the two. For MISO-induced intraseasonal variability, the ILD is controlled by diabetic ocean processes, i.e., the response of the ocean boundary layer to the strong surface warming/cooling from the atmosphere, whereas the change in thermocline depth is still largely the ocean wave adjustment to wind forcing, as indicated by Figures 12b and 12e. Our results reveal a high complexity of the ocean salinity stratification variability, which reminds caution for the future research.

Our simulation underestimates intraseasonal SSS anomaly in the northern bay, as compared with Aquarius data (Figure 11c), and the bias is much smaller in the southern bay (Figure 13c). This indicates a possible impact of intraseasonal river discharge of Ganga-Brahmaputra. Yet observational river discharge estimate at daily interval is still unavailable, which hinders a more realistic simulation of ocean salinity intraseasonal variability. Another potentially influential factor is the model resolution. Insufficient model resolution precludes some physical processes. Particularly, observed salinity profile is of complicated structure near the sea surface [e.g., *Felton et al*., 2014; *Song et al*., 2015; *Drushka et al*., 2016], which cannot be properly reproduced by the present vertical resolution (~2.9 m for the top layer). In addition, mesoscale eddies and submesoscale filaments are also important in modulating intraseasonal salinity variability in the far northern part of the bay [*Parampil et al*., 2010; *Sengupta et al*., 2016], requiring finer horizontal and vertical resolutions to take into account. Improvements in both in situ observation and numerical models are required to provide a more accurate interpretation of the complex salinity-related ocean processes in this region. Nevertheless, the present paper provides the first reliable understanding for the large-scale intraseasonal variability of MLD and BLT in the BoB, which builds a solid foundation for exploring the ocean salinity stratification's effect on MISO variability. Whether and to what extent the shallow MLD and large BLT can affect SST and convection of the MISO is of great interest for both the scientific community and the society. This effect will be investigated in Part 2 of the study.

Acknowledgments
Insightful comments from two anonymous reviewers are helpful for improving our work. The authors gratefully acknowledge the financial support given by the Earth System Science Organization, Ministry of Earth Sciences, Government of India (grant SSC-03–002; Project No. MM/SERP/CNRS/2013/INT-10/002) to conduct this research under Monsoon Mission. The research is also supported by the NASA Ocean Salinity Science Team award NNX14AI82G, NASA Ocean Vector Wind Science Team award NNX14AM68G, and NSF OCE 1658132. T. Shinoda is supported by NOAA grant NA15OAR431074, NSF grants AGS 1347132 and OCE 1658218, and NASA Physical Oceanography Program award NNX17AH25G. We appreciate the National Center for Atmospheric Research (NCAR) CISL and the Office of Information Technology (OIT) of University of Colorado and for providing and maintaining the computational resource. In this study, the Argo float data profiles are provided by the Coriolis Global Data Acquisition Center of France through http://www.coriolis.eu.org; in situ observational data from the RAMA buoys are provided by the NOAA Pacific Marine Environmental Laboratory (PMEL) through the website http://www.pmel.noaa.gov/tao/index.shtml; WOA13 Version-2 temperature and salinity climatology is downloaded from the NOAA National Centers for Environmental Information (NCEI) through https://www.nodc.noaa.gov/OC5/woa13/; Aquarius/SAC-D Combined Active-Passive retrieval (CAP) version 4.0 SSS product is distributed by NASA Jet Propulsion Laboratory (JPL) distributed by PO.DAAC and accessible through the FTP site ftp://podaac-ftp.jpl.nasa.gov/allData/aquarius/; TRMM TMPA level 3B42 precipitation product is available at http://mirador.gsfc.nasa.gov/; CCMP v1.1 sea surface wind data are downloaded from NASA JPL website http://podaac.jpl.nasa.gov/; gridded ASCAT surface wind data are provided by Centre de Recherche et d'Exploitation Satellitaire (CERSAT) of IFREMER, France through the FTP site ftp://ftp.ifremer.fr/ifremer/cersat/products/; CERES radiation data are taken from the website http://ceres.larc.nasa.gov/; data processing and graphing work in this study are completed using a licensed Matlab program.

References

Achuthavarier, D., and V. Krishnamurthy (2011), Role of Indian and Pacific SST in Indian summer monsoon intraseasonal variability, *J. Clim.*, *24*(12), 2915–2930.

Annamalai, H., and M. J. Slingo (2001), Active/break cycles: diagnosis of the intraseasonal variability of the Asian Summer Monsoon, *Clim. Dyn.*, *18*(1), 85–102.

Atlas, R., R. N. Hoffman, J. Ardizzone, S. M. Leidner, J. C. Jusem, D. K. Smith, and D. Gombos (2010), A cross-calibrated, multiplatform ocean surface wind velocity product for meteorological and oceanographic applications, *Bull. Am. Meteorol. Soc.*, *92*(2), 157–174.

Bentamy, A., and D. Croize-Fillon (2012), Gridded surface wind fields from Metop/ASCAT measurements, *Int. J. Remote Sens.*, *33*(6), 1729–1754.

Chen, G., D. Wang, and Y. Hou (2012), The features and interannual variability mechanism of mesoscale eddies in the Bay of Bengal, *Cont. Shelf Res.*, *47*, 178–185.

Cheng, X., S. P. Xie, J. P. McCreary, Y. Qi, and Y. Du (2013), Intraseasonal variability of sea surface height in the Bay of Bengal, *J. Geophys. Res. Oceans*, *118*, 816–830, doi:10.1002/jgrc.20075.

Dai, A., T. Qian, K. E. Trenberth, and J. D. Milliman (2009), Changes in continental freshwater discharge from 1948 to 2004, *J. Clim.*, *22*(10), 2773–2792.

de Boyer Montégut, C., G. Madec, A. S. Fischer, A. Lazar, and D. Iudicone (2004), Mixed layer depth over the global ocean: An examination of profile data and a profile-based climatology, *J. Geophys. Res.*, *109*, C12003, doi:10.1029/2004JC002378.

de Boyer Montégut, C., J. Mignot, A. Lazar, and S. Cravatte (2007), Control of salinity on the mixed layer depth in the world ocean: 1. General description, *J. Geophys. Res.*, *112*, C06011, doi:10.1029/2006JC003953.

Dee, D., et al. (2011), The ERA-interim reanalysis: Configuration and performance of the data assimilation system, *Q. J. R. Meteorol. Soc.*, *137*, 553–597.

Drushka, K., J. Sprintall, and S. T. Gille (2014), Subseasonal variations in salinity and barrier-layer thickness in the eastern equatorial Indian Ocean, *J. Geophys. Res. Oceans*, *119*, 805–823, doi:10.1002/2013JC009422.

Drushka, K., W. E. Asher, B. Ward, and K. Walesby (2016), Understanding the formation and evolution of rain-formed fresh lenses at the ocean surface, *J. Geophys. Res. Oceans*, *121*, 2673–2689, doi:10.1002/2015JC011527.

Duncan, B., and W. Han (2009), Indian Ocean intraseasonal sea surface temperature variability during boreal summer: Madden-Julian Oscillation versus submonthly forcing and processes, *J. Geophys. Res.*, *114*, C05002, doi:10.1029/2008JC004958.
Duvel, J. P., and J. Vialard (2007), Indo-Pacific sea surface temperature perturbations associated with intraseasonal oscillations of tropical convection, *J. Clim.*, *20*(13), 3056–3082.
Felton, C. S., B. Subrahmanyam, V. S. N. Murty, and J. F. Shriver (2014), Estimation of the barrier layer thickness in the Indian Ocean using Aquarius Salinity, *J. Geophys. Res. Oceans*, *119*, 4200–4213, doi:10.1002/2013JC009759.
Fu, X., and B. Wang (2004), Differences of boreal summer intraseasonal oscillations simulated in an atmosphere–ocean coupled model and an atmosphere-only model, *J. Clim.*, *17*(6), 1263–1271.
Fu, X., B. Wang, and T. Li (2002), Impacts of air–sea coupling on the simulation of mean Asian summer monsoon in the ECHAM4 model, *Mon. Weather Rev.*, *130*(12), 2889–2904.
Fu, X., B. Wang, T. Li, and J. P. McCreary (2003), Coupling between northward-propagating, intraseasonal oscillations and sea surface temperature in the Indian Ocean, *J. Atmos. Sci.*, *60*(15), 1733–1753.
Fu, X., B. Yang, Q. Bao, and B. Wang (2008), Sea surface temperature feedback extends the predictability of tropical intraseasonal oscillation, *Mon. Weather Rev.*, *136*(2), 577–597.
Gadgil, S., and K. Rupa Kumar (2006), The Asian monsoon—Agriculture and economy, in *The Asian Monsoon*, pp. 651–683, Springer, Berlin.
Girishkumar, M., M. Ravichandran, M. McPhaden, and R. Rao (2011), Intraseasonal variability in barrier layer thickness in the south central Bay of Bengal, *J. Geophys. Res.*, *116*, C03009, doi:10.1029/2010JC006657.
Girishkumar, M. S., M. Ravichandran, and W. Han (2013), Observed intraseasonal thermocline variability in the Bay of Bengal, *J. Geophys. Res. Oceans*, *118*, 3336–3349, doi:10.1002/jgrc.20245.
Gopalan, A., V. Krishna, M. Ali, and R. Sharma (2000), Detection of Bay of Bengal eddies from TOPEX and in situ observations, *J. Mar. Res.*, *58*(5), 721–734.
Goswami, B. N., and R. S. Ajaya Mohan (2001), Intraseasonal oscillations and interannual variability of the Indian summer monsoon, *J. Clim.*, *14*(6), 1180–1198.
Guan, B., T. Lee, D. J. Halkides, and D. E. Waliser (2014), Aquarius surface salinity and the Madden-Julian Oscillation: The role of salinity in surface layer density and potential energy, *Geophys. Res. Lett.*, *41*, 2858–2869, doi:10.1002/2014GL059704.
Halliwell, G. R. (2004), Evaluation of vertical coordinate and vertical mixing algorithms in the HYbrid-Coordinate Ocean Model (HYCOM), *Ocean Modell.*, *7*, 285–322.
Han, W., and J. P. McCreary (2001), Modeling salinity distributions in the Indian Ocean, *J. Geophys. Res.*, *106*(C1), 859–877.
Han, W., and P. J. Webster (2002), Forcing mechanisms of sea level interannual variability in the Bay of Bengal, *J. Phys. Oceanogr.*, *32*, 216–239.
Huang, C. J., F. Qiao, and D. Dai (2014), Evaluating CMIP5 simulations of mixed layer depth during summer, *J. Geophys. Res. Oceans*, *119*, 2568–2582, doi:10.1002/2013JC009535.
Huffman, G. J., D. T. Bolvin, E. J. Nelkin, D. B. Wolff, R. F. Adler, G. Gu, Y. Hong, K. P. Bowman, and E. F. Stocker (2007), The TRMM multisatellite precipitation analysis (TMPA): Quasi-global, multiyear, combined-sensor precipitation estimates at fine scales, *J. Hydrometeorol.*, *8*(1), 38–55.
Hoyos, C. D., and P. J. Webster (2007), The role of intraseasonal variability in the nature of Asian monsoon precipitation, *J. Clim.*, *20*(17), 4402–4424.
Jochum, M., and R. Murtugudde (2005), Internal variability of Indian Ocean SST, *J. Clim.*, *18*(18), 3726–3738.
Joseph, P. V., and T. P. Sabin (2008), An ocean–atmosphere interaction mechanism for the active break cycle of the Asian summer monsoon, *Clim. Dyn.*, *30*(6), 553–566.
Kara, A. B., H. E. Hurlburt, and A. J. Wallcraft (2005), Stability-dependent exchange coefficients for air-sea fluxes, *J. Atmos. Oceanic Technol.*, *22*(7), 1080–1094.
Keerthi, M. G., M. Lengaigne, K. Drushka, J. Vialard, C. de Boyer Montegut, S. Pous, M. Levy, and P. M. Muraleedharan (2016), Intraseasonal variability of mixed layer depth in the tropical Indian Ocean, *Clim. Dyn.*, *46*(7), 2633–2655.
Keerthi, M., M. Lengaigne, J. Vialard, C. de Boyer Montégut, and P. Muraleedharan (2013), Interannual variability of the Tropical Indian Ocean mixed layer depth, *Clim. Dyn.*, *40*(3-4), 743–759.
Kemball-Cook, S., and B. Wang (2001), Equatorial waves and air–sea interaction in the boreal summer intraseasonal oscillation, *J. Clim.*, *14*(13), 2923–2942.
Krishnamurti, T. N., and D. Subrahmanyam (1982), The 30–50 day mode at 850 mb during MONEX, *J. Atmos. Sci.*, *39*(9), 2088–2095.
Kurien, P., M. Ikeda, and V. K. Valsala (2010), Mesoscale variability along the east coast of India in spring as revealed from satellite data and OGCM simulations, *J. Oceanogr.*, *66*(2), 273–289.
Lagerloef, G., F. R. Colomb, D. Le Vine, F. Wentz, S. Yueh, C. Ruf, J. Lilly, J. Gunn, Y. Chao, and A. deCharon (2008), The aquarius/SAC-D mission: Designed to meet the salinity remote-sensing challenge, *Oceanography*, *21*(1), 68–81.
Lau, K. M., and S. Yang (1996), Seasonal variation, abrupt transition, and intraseasonal variability associated with the Asian summer monsoon in the GLA GCM, *J. Clim.*, *9*(5), 965–985.
Lebedev, K. V., H. Yoshinari, N. A. Maximenko, and P. W. Hacker (2007), Velocity data assessed from trajectories of Argo floats at parking level and at the sea surface, *IPRC Tech. Note*, *4*(2), 1–16.
Li, Y., and W. Han (2016), Causes for intraseasonal sea surface salinity variability in the western tropical Pacific Ocean and its seasonality, *J. Geophys. Res. Oceans*, *121*, 85–103, doi:10.1002/2015JC011413.
Li, Y., W. Han, T. Shinoda, C. Wang, R. C. Lien, J. N. Moum, and J. W. Wang (2013), Effects of the diurnal cycle in solar radiation on the tropical Indian Ocean mixed layer variability during wintertime Madden-Julian Oscillations, *J. Geophys. Res. Oceans*, *118*, 4945–4964, doi:10.1002/jgrc.20395.
Li, Y., W. Han, T. Shinoda, C. Wang, M. Ravichandran, and J.-W. Wang (2014), Revisiting the wintertime intraseasonal SST variability in the tropical South Indian Ocean: Impact of the ocean interannual variation, *J. Phys. Oceanogr.*, *44*(7), 1886–1907.
Li, Y., W. Han, and T. Lee (2015), Intraseasonal sea surface salinity variability in the equatorial Indo-Pacific Ocean induced by Madden-Julian oscillations, *J. Geophys. Res. Oceans*, *120*, 2233–2258, doi:10.1002/2014JC010647.
Li, Y., W. Han, W. Wang, and M. Ravichandran (2016), Intraseasonal variability of SST and precipitation in the Arabian Sea during Indian summer monsoon: Impact of the ocean mixed layer depth, *J. Clim.*, *29*(21), 7889–7910.
Li, Y., W. Han, W. Wang, M. Ravichandran, T. Lee, and T. Shinoda (2017), Bay of Bengal salinity stratification and Indian summer monsoon intraseasonal oscillation: 2. Impact on SST and convection, *J. Geophys. Res. Oceans*, doi:10.1002/2017JC012692, in press.
Locarnini, R. A., et al. (2013), World ocean atlas 2013: Temperature, in *NOAA Atlas NESDIS 73*, vol. 1, edited by S. Levitus and A. Mishonov, 40 pp., Silver Spring, Md.

Loeb, N. G., K. J. Priestley, D. P. Kratz, E. B. Geier, R. N. Green, B. A. Wielicki, P. O. R. Hinton, and S. K. Nolan (2001), Determination of unfiltered radiances from the clouds and the Earth's radiant energy system instrument, *J. Appl. Meteorol.*, *40*(4), 822–835.

Matthews, A. J., P. Singhruck, and K. J. Heywood (2010), Ocean temperature and salinity components of the Madden–Julian oscillation observed by Argo floats, *Clim. Dyn.*, *35*, 1149–1168.

McPhaden, M. J., G. Meyers, K. Ando, Y. Masumoto, V. S. N. Murty, M. Ravichandran, F. Syamsudin, J. Vialard, L. Yu, and W. Yu (2009), RAMA: The research moored array for African–Asian–Australian monsoon analysis and prediction, *Bull. Am. Meteorol. Soc.*, *90*(4), 459–480.

Neetu, S., M. Lengaigne, E. M. Vincent, J. Vialard, G. Madec, G. Samson, M. R. Ramesh Kumar, and F. Durand (2012), Influence of upper-ocean stratification on tropical cyclone-induced surface cooling in the Bay of Bengal, *J. Geophys. Res.*, *117*, C12020, doi:10.1029/2012JC008433.

Owens, W. B., and A. P. S. Wong (2009), An improved calibration method for the drift of the conductivity sensor on autonomous CTD profiling floats by θ–*S* climatology, *Deep Sea Res., Part I*, *56*(3), 450–457.

Papa, F., F. Durand, W. B. Rossow, A. Rahman, and S. K. Bala (2010), Satellite altimeter-derived monthly discharge of the Ganga-Brahmaputra River and its seasonal to interannual variations from 1993 to 2008, *J. Geophys. Res.*, *115*, C12013, doi:10.1029/2009JC006075.

Parampil, S. R., A. Gera, M. Ravichandran, and D. Sengupta (2010), Intraseasonal response of mixed layer temperature and salinity in the Bay of Bengal to heat and freshwater flux, *J. Geophys. Res.*, *115*, C05002, doi:10.1029/2009JC005790.

Parthasarathy, B., A. A. Munot, and D. R. Kothawale (1994), All-India monthly and seasonal rainfall series: 1871–1993, *Theor. Appl. Climatol.*, *49*(4), 217–224.

Rajendran, K., and A. Kitoh (2006), Modulation of tropical intraseasonal oscillations by ocean–atmosphere coupling, *J. Clim.*, *19*(3), 366–391.

Rao, R., M. G. Kumar, M. Ravichandran, A. Rao, V. Gopalakrishna, and P. Thadathil (2010), Interannual variability of Kelvin wave propagation in the wave guides of the equatorial Indian Ocean, the coastal Bay of Bengal and the southeastern Arabian Sea during 1993–2006, *Deep Sea Res., Part I*, *57*, 1–13.

Rao, R. R., and R. Sivakumar (2003), Seasonal variability of sea surface salinity and salt budget of the mixed layer of the north Indian Ocean, *J. Geophys. Res.*, *108*(C1), 3009, doi:10.1029/2001JC000907.

Roemmich, D. H., G. C. Johnson, S. Riser, R. Davis, J. Gilson, W. B. Owens, S. L. Garzoli, C. Schmid, and M. Ignaszewski (2009), The Argo program: Observing the global ocean with profiling floats, *Oceanography*, *22*, 34–43.

Roxy, M., Y. Tanimoto, B. Preethi, P. Terray, and R. Krishnan (2013), Intraseasonal SST-precipitation relationship and its spatial variability over the tropical summer monsoon region, *Clim. Dyn.*, *41*, 45–61.

Schiller, A., and J. Godfrey (2005), A diagnostic model of the diurnal cycle of sea surface temperature for use in coupled ocean-atmosphere models, *J. Geophys. Res.*, *110*, C11014, doi:10.1029/2005JC002975.

Sengupta, D., and M. Ravichandran (2001), Oscillations of Bay of Bengal sea surface temperature during the 1998 summer monsoon, *Geophys. Res. Lett.*, *28*(10), 2033–2036.

Sengupta, D., B. N. Goswami, and R. Senan (2001), Coherent intraseasonal oscillations of ocean and atmosphere during the Asian summer monsoon, *Geophys. Res. Lett.*, *28*(21), 4127–4130.

Sengupta, D., G. N. Bharath Raj, M. Ravichandran, J. Sree Lekha, and F. Papa (2016), Near-surface salinity and stratification in the north Bay of Bengal from moored observations, *Geophys. Res. Lett.*, *43*, 4448–4456, doi:10.1002/2016GL068339.

Shenoi, S. S. C., D. Shankar, and S. R. Shetye (2002), Differences in heat budgets of the near-surface Arabian Sea and Bay of Bengal: Implications for the summer monsoon, *J. Geophys. Res.*, *107*(C6), 3052, doi:10.1029/2000JC000679.

Seo, K.-H., J.-K. E. Schemm, W. Wang, and A. Kumar (2007), The boreal summer intraseasonal oscillation simulated in the NCEP climate forecast system: The effect of sea surface temperature, *Mon. Weather Rev.*, *135*(5), 1807–1827.

Song, Y. T., T. Lee, J.-H. Moon, T. Qu, and S. Yueh (2015), Modeling skin-layer salinity with an extended surface-salinity layer, *J. Geophys. Res. Oceans*, *120*, 1079–1095, doi:10.1002/2014JC010346.

Sprintall, J., and M. Tomczak (1992), Evidence of the barrier layer in the surface layer of the tropics, *J. Geophys. Res.*, *97*(C5), 7305–7316.

Thadathil, P., P. M. Muraleedharan, R. R. Rao, Y. K. Somayajulu, G. V. Reddy, and C. Revichandran (2007), Observed seasonal variability of barrier layer in the Bay of Bengal, *J. Geophys. Res.*, *112*, C02009, doi:10.1029/2006JC003651.

Thadathil, P., I. Suresh, S. Gautham, S. Prasanna Kumar, M. Lengaigne, R. R. Rao, S. Neetu, and A. Hegde (2016), Surface layer temperature inversion in the Bay of Bengal: Main characteristics and related mechanisms, *J. Geophys. Res. Oceans*, *121*, 5682–5696, doi:10.1002/2016JC011674.

Turner, A. G., and H. Annamalai (2012), Climate change and the South Asian summer monsoon, *Nat. Clim. Change*, *2*(8), 587–595.

Turner, A. G., M. Joshi, E. S. Robertson, and S. J. Woolnough (2012), The effect of Arabian Sea optical properties on SST biases and the South Asian summer monsoon in a coupled GCM, *Clim. Dyn.*, *39*(3), 811–826.

Vecchi, G. A., and D. E. Harrison (2002), Monsoon breaks and subseasonal sea surface temperature variability in the Bay of Bengal, *J. Clim.*, *15*(12), 1485–1493.

Vialard, J., A. Jayakumar, C. Gnanaseelan, M. Lengaigne, D. Sengupta, and B. Goswami (2012), Processes of 30–90 days sea surface temperature variability in the northern Indian Ocean during boreal summer, *Clim. Dyn.*, *38*, 1901–1916.

Vinayachandran, P. N., V. S. N. Murty, and V. Ramesh Babu (2002), Observations of barrier layer formation in the Bay of Bengal during summer monsoon, *J. Geophys. Res.*, *107*(C12), 8018, doi:10.1029/2001JC000831.

Vinayachandran, P. N., D. Shankar, S. Vernekar, K. K. Sandeep, P. Amol, C. P. Neema, and A. Chatterjee (2013), A summer monsoon pump to keep the Bay of Bengal salty, *Geophys. Res. Lett.*, *40*, 1777–1782, doi:10.1002/grl.50274.

Waliser, D. E., Z. Zhang, K. Lau, and J. H. Kim (2001), Interannual sea surface temperature variability and the predictability of tropical intraseasonal variability, *J. Atmos. Sci.*, *58*(17), 2596–2615.

Waliser, D. E., R. Murtugudde, and L. E. Lucas (2004), Indo-Pacific Ocean response to atmospheric intraseasonal variability: 2. Boreal summer and the intraseasonal oscillation, *J. Geophys. Res*, *109*, C03030, doi:10.1029/2003JC002002.

Wang, B., and X. Xie (1997), A model for the boreal summer intraseasonal oscillation, *J. Atmos. Sci.*, *54*(1), 72–86.

Wang, B., Q. Ding, X. Fu, I.-S. Kang, K. Jin, J. Shukla, and F. Doblas-Reyes (2005), Fundamental challenge in simulation and prediction of summer monsoon rainfall, *Geophys. Res. Lett.*, *32*, L15711, doi:10.1029/2005GL022734.

Wang, W., M. Chen, and A. Kumar (2009), Impacts of ocean surface on the northward propagation of the boreal summer intraseasonal oscillation in the NCEP climate forecast system, *J. Clim.*, *22*(24), 6561–6576.

Webster, P. J., V. Magaa, T. Palmer, J. Shukla, R. Tomas, M. U. Yanai, and T. Yasunari (1998), Monsoons: Processes, predictability, and the prospects for prediction, *J. Geophys. Res.*, *103*(C7), 14,451–14,510.

Webster, P. J., et al. (2002), The JASMINE pilot study, *Bull. Am. Meteorol. Soc.*, *83*, 1603–1630.

Wielicki, B. A., B. R. Barkstrom, E. F. Harrison, R. B. Lee III, G. Louis Smith, and J. E. Cooper (1996), Clouds and the Earth's radiant energy system (CERES): An earth observing system experiment, *Bull. Am. Meteorol. Soc.*, *77*(5), 853–868.

Yasunari, T. (1980), A quasi-stationary appearance of 30 to 40 day period in the cloudiness fluctuations during the summer monsoon over India, *J. Meteorol. Soc. Jpn.*, *58*, 225–229.

Yueh, S., W. Tang, A. Fore, A. Hayashi, Y. T. Song, and G. Lagerloef (2014), Aquarius geophysical model function and combined active passive algorithm for ocean surface salinity and wind retrieval, *J. Geophys. Res. Oceans*, *119*(8), 5360–5379, doi:10.1002/2014jc009939.

Zweng, M. M., et al. (2013), World ocean atlas 2013: Salinity, in *NOAA Atlas NESDIS 74*, vol. 2, edited by S. Levitus and A. Mishonov, 39 pp, Silver Spring, Md.